Characterization of Fluorohydrogenated Ionic Liquids for Use in the Ion Electrospray Propulsion System

by

Caroline Lee Bates

B.S., Astronautical Engineering,
United States Air Force Academy (2016)

Submitted to the Department of Aeronautics and Astronautics
in partial fulfillment of the requirements for the degree of

Master of Science in Aeronautics and Astronautics

at the

MASSACHUSETTS INSTITUTE OF TECHNOLOGY

June 2018

© Massachusetts Institute of Technology 2018. All rights reserved.

Author . . . .

Signature redacted

Department of Aeronautics and Astronautics
May 24, 2018

Certified by . . . .

Signature redacted

Paulo C. Lozano
Professor of Aeronautics and Astronautics
Thesis Supervisor

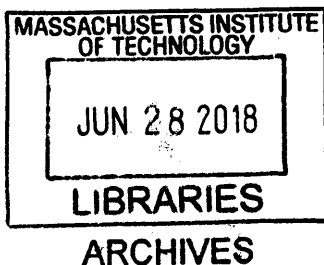Accepted by . . . .

Signature redacted

Hamsa Balakrishnan
Associate Professor of Aeronautics and Astronautics
Chair, Graduate Program Committee

Disclaimer: The views expressed in this thesis are those of the author and do not reflect the official policy or position of the United States Air Force, the United States Department of Defense, or the United States Government.

Characterization of Fluorohydrogenated Ionic Liquids for Use in the Ion Electrospray Propulsion System

by

Caroline Lee Bates

Submitted to the Department of Aeronautics and Astronautics
on May 24, 2018, in partial fulfillment of the
requirements for the degree of
Master of Science in Aeronautics and Astronautics

Abstract

This thesis investigates the use of two fluorohydrogenated ionic liquids as propellants for the ion Electrospray Propulsion System developed at MIT, 1-ethyl-3-methylimidazolium fluorohydrogenate and trimethylsulfonium fluorohydrogenate. It was found that these ionic liquids undergo a crystallization-like transformation when exposed to vacuum for several hours. Mixtures with a vacuum stable ionic liquid (1-ethyl-3-methylimidazolium trifluoro(trifluoro methyl)borate) were made to study the onset of this transformation and to obtain liquid mixtures from which stable electrospray emission could be obtained. Mixtures containing 10%, 25%, or 50% by mass of one of the fluorohydrogenated ionic liquids are then investigated using time of flight mass spectrometry to determine the beam compositions. All six mixtures operate in the pure ionic regime. Of the six mixtures, the mixture of 25% trimethlysulfonium fluorohydrogenate is the best candidate for use as propellant in the ion Electrospray Propulsion System, because it produces current 4.8 times higher than pure 1-ethyl-3-methylimidazolium trifluoro(trifluoro methyl)borate, and the beam is composed entirely of monomers. Additionally, at voltages used for the ion Electrospray Propulsion System, the 25% trimethlysulfonium fluorohydrogenate mixture has an increase in specific impulse up to 2,000 s over pure 1-ethyl-3-methylimidazolium trifluoro(trifluoro methyl)borate. In the appendix, an application of the ion Electrospray Propulsion System is investigated, namely the new WaferSat femtosatellite being developed at MIT Lincoln Laboratory. Motion simulations give preliminary insights into how WaferSats will move in orbit.

Thesis Supervisor: Paulo C. Lozano
Title: Professor of Aeronautics and Astronautics

Acknowledgments

Above all, I give my thanks and gratitude to my God, Father, Son, and Holy Spirit. I thank You for the opportunity to study at MIT and for sustaining me throughout my time here. I also thank You for my parish family at St. Nicholas GOC and for Fr. Demetri who heard my Confession during my time at MIT. Lord Jesus Christ, Son of God, have mercy on me, a sinner! I also thank the Theotokos and St. Catherine the Greatmartyr of Alexandria for their intercessions on my behalf.

Next, I would like to thank my advisors and mentors at MIT SPL and MIT Lincoln Laboratory, Prof. Paulo Lozano and Dr. Joseph Vornehm. To Prof. Lozano, thank you for the opportunity to work in SPL and for always being willing to help me when I had questions. To Joe Vornehm, thank you for your friendship, for helping me with coding, and for helping me to navigate the transition between undergraduate and graduate student research. I am deeply grateful to my Lincoln Laboratory Group Leader Dr. Kathleen Bihari for welcoming me into her Group and providing the funding necessary for me to attend MIT. I am also indebted to Catherine Miller for the use of her time of flight setup.

Last, but not least, I would like to thank my mom. Thank you for your support, for always answering my phone calls, and for listening to my complaining about my "problem liquids."

Contents

List of Figures

List of Tables

Chapter 1

Introduction

Miniature satellites are growing in popularity in the space community. These satellites are very small and lightweight compared to traditional satellites. Nanosatellites weigh between 1 and 10 kg, and pico- and femtosats are even smaller. Historically, these tiny satellites have lacked propulsion systems. Chemical propulsion cannot be scaled down to the necessary size, and most types of electric propulsion become too inefficient at the sizes needed by nano- and smaller satellites. One promising propulsion option for miniature satellites is the ion electrospray propulsion system (iEPS) developed by the MIT Space Propulsion Laboratory (SPL). The iEPS has high specific impulse, and is scalable to sizes suitable for these satellites.

The purpose of this research is to investigate two fluorohydrogenated ionic liquids (FHILs) for use as propellants in the iEPS. Currently, an iEPS thruster provides thrust on the order of 10 nN per emitter tip. The current iteration of the iEPS thruster array produces 12.5 µN of thrust from 480 emitter tips in 1 cm^2. SPL is seeking to improve the performance of iEPS thrusters by increasing the thrust density. There are two main ways to increase the thrust density of an electrospray thruster. First, the emitter tips in the array can be placed closer together, and therefore have more thrust-producing emitter tips in the same size thruster array. However, there are physical limits to how close emitter tips can be to each other, both in terms of machining ability and how close emitter tips can be before they interact via surface tension and/or electric forces. The second method to increase thrust is to increase the

conductivity of the ionic liquid [1]. As shown later in the text, the emitted current I is linearly dependent on electrical conductivity, K, as given by $I = K \left(\frac{32\pi\gamma^2}{\epsilon_0 E^{*3}} \right) \left(\frac{\epsilon}{(\epsilon-1)^2} \right)$ where ϵ_0 is the permittivity of vacuum, ϵ is the dielectric constant of the ionic liquid, γ is the liquid surface tension, and E^* is the critical electric field for current emission [2]. Higher emitted currents will result in higher thrust densities. Conventional fuels for iEPS, including 1-ethyl-3-methylimidazolium tetrafluoroborate (EMI-BF$_4$) and 1-ethyl-3-methylimidazolium bis(trifluoromethylsulfonyl)imide (EMI-Im), have electrical conductivities of $K \sim 1$ S/m [1]. In order to increase the electrical conductivity at constant temperature another ionic liquid must be used. FHILs display most of the attributes of conventional ionic liquids, like low vapor pressures, but have much higher electrical conductivities. The two FHILs investigated in this thesis are 1-ethyl-3-methylimidazolium fluorohydrogenate (EMI-(HF)$_{2.3}$F) and trimethyl-sulfonium fluorohydrogenate (S$_{111}$-(HF)$_{1.9}$F), with electrical conductivities of $K = 10$ S/m and $K = 13.1$ S/m, respectively [3, 4]. These two FHILs are predicted then to provide current an order of magnitude higher than with the current propellants used in iEPS thrusters. This would put the thrust density of iEPS in line with low-power Hall thrusters [5]. In order to achieve a similar increase in thrust density by modify-
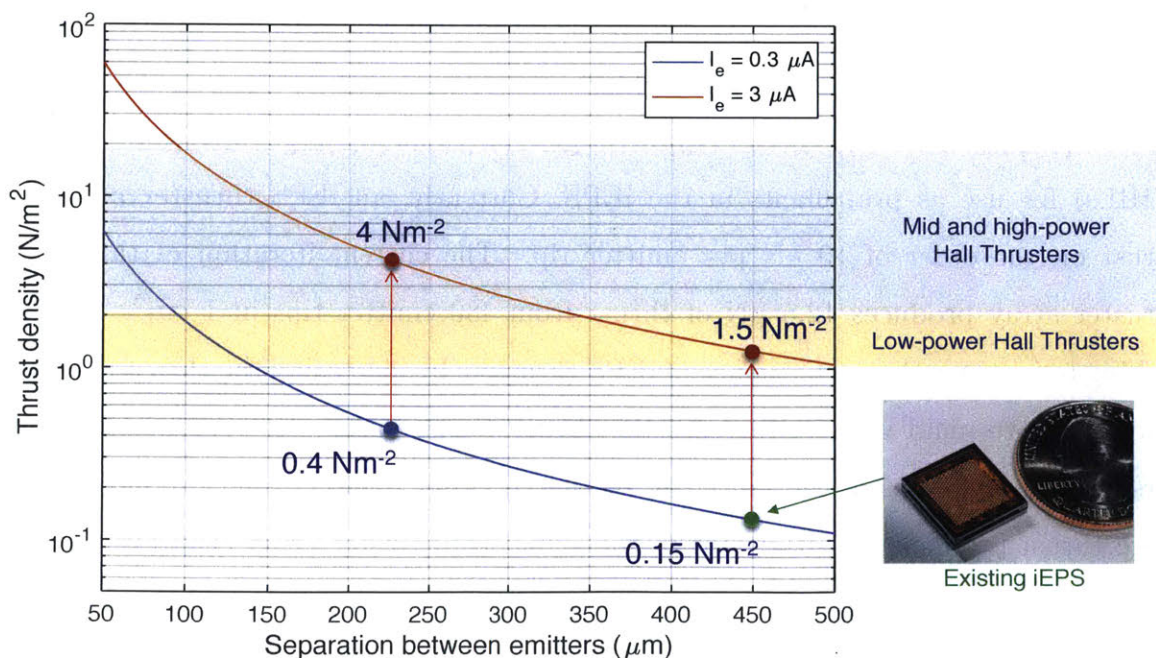

Figure 1-1: Thrust density of iEPS compared to Hall thrusters.

ing the spacing between emitter tips, they would have to be placed $\sqrt{10}$ times closer together [6]. Changing the iEPS propellant from EMI-BF$_4$ to either EMI-(HF)$_{2.3}$F or S$_{111}$-(HF)$_{1.9}$F is expected to produce the ten-fold increase in thrust density without redesigning the iEPS array.

1.1 Background

Electrospray propulsion is a form of electric propulsion that operates by electrostatically accelerating charged particles from electrified liquid fuel sources. Unlike other forms of electric propulsion, electrosprays do not need to have a volume for gas phase ionization. This allows electrospray thrusters to be relatively small. In contrast, miniaturizing other forms of electric propulsion, such as Hall thrusters, ion thrusters, and arcjets, increases the heat and energetic ion fluxes to the walls of the thrusters; this decreases the efficiency and life of the thruster [7].

The first form of electrospray propulsion to be developed was the colloid thruster. Researchers studied these devices between 1960 and 1975 as a possible alternative to ion engines. Colloid thrusters work by accelerating charged droplets, and under special circumstances, ions. They use solvents such as doped glycerol and formamide as propellant. The large molecular mass of the droplets in colloid thrusters appealed to researchers, because in ion engines, a larger molecular mass increases the thrust density of the engine. The colloid thruster research provided useful results, with some being capable of producing a specific impulse, I_{sp}, of approximately 1000 s at accelerating voltages between 10 and 100 kV. However, the high voltages made the colloid thrusters difficult to insulate and package, so they were undesirable for use on spacecraft despite being successful on the ground. Additionally, each individual capillary in the colloid thrusters produced approximately 1 μN of thrust. Therefore, in order to produce the amount of thrust for the spacecraft missions anticipated at the time, the arrays of capillaries would have had to be very large [7].

Although the colloid thruster research of the mid-twentieth century was abandoned, new research into electrospray propulsion has begun within the past two

decades. This time, the emphasis is on developing propulsion for the new nano- and picosatellites (satellites roughly 10 kg in mass and smaller). In these tiny satellites, the small thrust per emitter that was previously a drawback of the colloid thruster is now an advantage, allowing for fine control of a satellite and higher thruster performance. Furthermore, research in the field of electrospray science since the 1970s now allows for electrosprays to operate at more feasible voltages of 1 to 5 kV. Finally, improvements in micro-manufacturing now allow for a large number of emitters to be fabricated on a very small surface. These advances make possible the miniaturization of electrosprays. At the MIT Space Propulsion Laboratory, research is being conducted into electrosprays fueled by ionic liquid ion sources, in particular the ion Electrospray Propulsion System (iEPS)[7].

Ionic liquids are also known as room temperature molten salts. They are composed of highly asymmetrical molecular ions that do not form crystalline structures at room temperature. Rather, they are a sea of ions that remain in the liquid state without the presence of a solvent. They are useful in space propulsion for a variety of reasons. Most ionic liquids have practically no vapor pressure, which makes them easy to store in space. Additionally, since ionic liquids naturally consist of free ions, a propulsion system using an ionic liquid as propellant does not need an ionization stage, allowing the propulsion system to be efficient and compact. Most importantly, the electrical conductivity of ionic liquids means that they can be electrically stressed, and thereby produce electrospray emission [8].

The basic unit of the iEPS electrospray thruster is the single porous emitter. Ionic liquid propellant is held in a reservoir below the emitter. Capillary action pulls the ionic liquid through pores in the emitter and to the tip. Above the emitter tip, an extractor plate applies an electric field at the liquid-vacuum interface, forming a meniscus that collapses into a structure usually called a Taylor Cone [9]. Depending on flow rate, emission could consist of mixtures of ions and droplets or only ions [10].

Romero-Sanz, Bocanegra, and Fernandez de la Mora were the first to discover that ionic liquids could produce emissions composed only of ions without the pres-
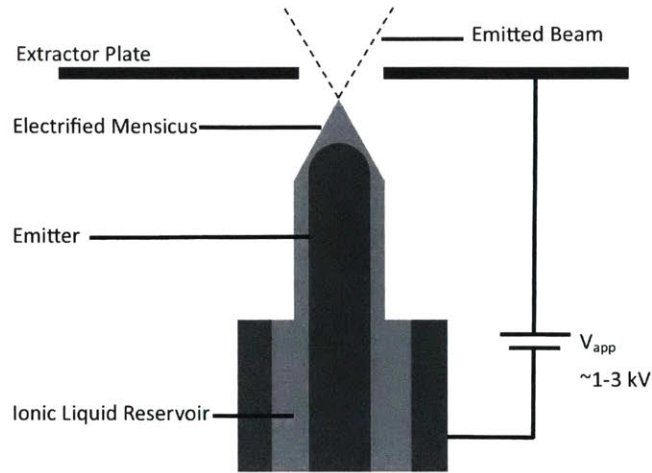
Figure 1-2: A single porous emitter, adapted from Ref. [10].

ence of droplets [11]. The so-called pure ionic regime (PIR) is the most interesting one as it maximizes efficiency and specific impulse at moderate extraction voltage. The presence of droplets in the mixed ion-droplet regime reduces the efficiency considerably. In the pure ionic mode, individual ions field-evaporate from the tip of the cone, are accelerated by the electric field, and pass through a hole in the extractor plate. Within the PIR, ions can either be single ions, called monomers, or larger ions such as dimers and trimers (single ions attached to one or two neutral particles, respectively). Emission of only monomers is the most efficient and therefore the most beneficial for space propulsion. A beam consisting of multiple species of charged particles suffers efficiency losses due to polydispersity. All of the charged particle species in the beam have the same energy, but larger species have slower velocites. As shown in the next section, thrust is linearly dependent on the velocites of the charged particles, so slower velocites result in less thrust [12].

Each individual iEPS emitter provides thrust on the order of 10 nN. In order to produce sufficient thrust for a spacecraft mission, many emitters are arranged together into an array. Currently iEPS arrays contain 480 emitters in a 1 cm^2 array, producing 12 µN of thrust [1]. Use of FHILs as propellant should increase the thrust provided by an iEPS array for the same emitter density.

1.2 Ion Evaporation from Ionic Liquids

Electrospray propulsion operates by emitting ions from the surface of the ionic liquid propellant. However, ionic liquids have a high energy barrier for ion evaporation. In some cases, the free energy of solvation to extract ions can be as high as 1.5 eV. This energy barrier can be reduced, however, by applying an electric field normal to the surface of the liquid. The equation for the field-evaporated current density is

$$j = \sigma \left(\frac{kT}{h} \right) exp \left[-\frac{1}{kT} \left(\Delta G - G(E) \right) \right].$$
(1.1)

Here ΔG is the free energy of solvation, $G(E)$ is the reduction of the free energy of solvation due to the normal electric field, σ is the surface charge density, k is the Bolzmann's constant, T is the temperature, and h is Planck's constant. Current emission is possible when $G(E)$ approaches ΔG. The reduction of the free energy of solvation, $G(E)$, is described by

$$G(E) = \sqrt{\frac{e^3 E}{4\pi\epsilon_0}}.$$
(1.2)

The critical electric field E^* for ion evaporation occurs when $G(E) \approx \Delta G$,

$$E^* \approx \frac{4\pi\epsilon_0}{e^3} \Delta G^2.$$
(1.3)

The value for E^* can be as high as 1.6 V/nm for some ionic liquids. Fortunately, it is not necessary to directly apply such a high electric field to the ionic liquid to operate an electrospray thruster [8].

If a large enough electric field is applied normal to the ionic liquid, the liquid deforms and collapses into a Taylor cone, illustrated in Figure 1-3. This Taylor cone is formed by the balance between the pressure caused by the electric field and the surface tension of the liquid, as shown by the equation

$$\frac{1}{2}\epsilon_0 E_n^2 = \frac{\gamma \cot \theta}{r},$$
(1.4)

where ϵ_0 is the permittivity of vacuum, E^n is the electric field acting normally on the liquid, γ is the surface tension of the liquid, θ is the angle of the Taylor cone, and r is the distance from the tip of the cone to a point on its surface. Equation 1.4 can be rewritten to find the normal electric field

$$E_n = \sqrt{\frac{2\gamma \cot\theta}{\epsilon_0 r}}. \tag{1.5}$$

[7] As r decreases, E_n increases; let $r = r^*$ be the distance that makes $E_n = E^*$, the critical field needed for ion evaporation [1].
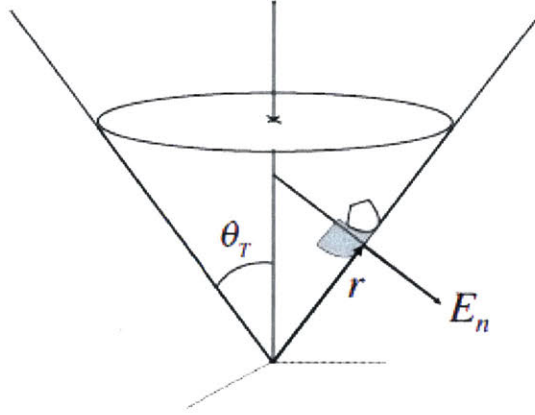
Figure 1-3: Taylor cone, from Ref. [7].

While theoretically the Taylor cone is a perfectly shaped cone, in reality it does not end in a sharp point. Rather, the meniscus that forms has a blunt structure with a curvature at its apex of $2/r^*$. For ionic liquids, the conductivity of the liquid is low enough that it forces the charge density to be far from fully relaxed ($\sigma \ll \epsilon_0 E^*$). The electric field inside the Taylor cone then is approximately $E_{in} \sim E^*/\epsilon$. For the case of equilibrium, the mechanical balance at the curved interface of the Taylor Cone is $\frac{1}{2}\epsilon_0 E^{*2} - \frac{1}{2}\epsilon_0 \epsilon E_{in}^2 \approx 2\gamma/r^*$, which gives

$$r^* \approx \left(\frac{4\gamma}{\epsilon_0 E^{*2}}\right)\left(\frac{\epsilon}{\epsilon - 1}\right). \tag{1.6}$$

Assuming a half-sphere current emission, the total current I is $I = 2jr^{*2}$ where j is the current density emitted from the surface of the meniscus. Neglecting convection, charge transport is due only to the liquid conductivity such that $j = KE_{in} \approx KE^*/\epsilon$. Thus, the emitted current becomes,

$$I \approx \left(\frac{32\pi K\gamma^2}{\epsilon_0^2 E^{*3}} \right) \frac{\epsilon}{\left(\epsilon - 1\right)^2}. \tag{1.7}$$

This linear relationship between emitted current and conductivity provides the motivation for this work. EMI-(HF)$_{2.3}$F and S$_{111}$-(HF)$_{1.9}$F have conductivities an order of magnitude higher than that of EMI-BF$_4$. Therefore, an electrospray thruster using either of these FHILs as fuel should have an emitted current up to an order of magnitude higher than an electrospray thruster using EMI-BF$_4$. Assuming the mean specific charge for emitted species is q/m, the ideal thrust produced by an electrospray emitter will be given by,

$$F = \dot{m}v = \left[\frac{I}{q/m} \right] \sqrt{2\frac{q}{m}V}, \tag{1.8}$$

where I is the current, and V is the applied voltage [13]. Thrust is proportional to current, which is proportional to conductivity. So, a thruster using EMI-(HF)$_{2.3}$F or S$_{111}$-(HF)$_{1.9}$F will provide thrust up to an order of magnitude greater than a thruster using EMI-BF$_4$ at similar voltages and charge-to-mass ratios, simply because of the higher conductivity of the FHILs.

Chapter 2

Research

2.1 "Crystallization" of FHILs in Vacuum

Both EMI-$(HF)_{2.3}F$ and S_{111}-$(HF)_{1.9}F$ in their pure forms adopt a "crystal"-like structure when exposed to vacuum. This is problematic for space propulsion as the propellant becomes unusable in its solid form. The high electrical conductivity of these ionic liquids, however, is anticipated to improve the thrust performance of iEPS.

(a) S_{111}-$(HF)_{1.9}F$ before vacuum.   (b) S_{111}-$(HF)_{1.9}F$ after 3 hours in vacuum.

Figure 2-1: Crystallization of S_{111}-$(HF)_{1.9}F$ in vacuum (in tip of dropper). Note the clear color of the liquid phase before vacuum, and the cloudy appearance due to crystal-like structure formation after 3 hours in vacuum.

Therefore, it was hypothesized that mixtures of these FHILs with ionic liquids that are known to be stable in vacuum might produce combinations that will remain as liquid while improving the conductivity. Initial experiments to determine the crystallization

boundaries of the FHILs used EMI-Im. However, EMI-Im was replaced by 1-ethyl-3-methylimidazolium trifluoro(trifluoro methyl) borate (EMI-CF$_3$BF$_3$), because of the higher conductivity of EMI-CF$_3$BF$_3$. This liquid has a conductivity of 1.46 Si/m at 25° C [14], similar to that of EMI-BF$_4$. EMI-CF$_3$BF$_3$ has a lower electrical conductivity than the two FHILs, but it has the advantage of remaining in a liquid state when exposed to vacuum. Since EMI-(HF)$_{2.3}$F and S$_{111}$-(HF)$_{1.9}$F have higher conductivities than EMI-CF$_3$BF$_3$, the mixtures should have as high a concentration of the FHILs as possible. Therefore, the first experiment to be done was to determine the highest possible concentration of each FHIL that can be mixed with EMI-CF$_3$BF$_3$ without the mixtures crystallizing.

Mass fractions of FHIL were chosen around the suspected crystallization boundary. Each mixture was placed in an individually marked Teflon dish. Each mixture had a mass of approximately 0.20 g. First, the desired mass of one of the FHILs, either EMI-(HF)$_{2.3}$F or S$_{111}$-(HF)$_{1.9}$F, was dropped in the Teflon dish using a syringe. Next, EMI-CF$_3$BF$_3$ was added to the Teflon dish to bring the total mixture mass to approximately 0.20 g. The Teflon dishes were then placed in a vacuum chamber for approximately two days, where the pressure was below 1×10^{-5} Torr. Throughout the two days, the mixtures were observed through a window in the vacuum chamber and any crystallization was recorded. Figure 2-2 shows photographs of actual FHIL mixtures in the possible degrees of crystallization, while Figure 2-3 shows an artistic impression of the same for the sake of clarity. There are five degrees of crystallization separated into three regions. The first degree is no crystallization, and occurs when the fraction of FHIL in the mixture is below the crystallization transition region. The next three degrees of crystallization occur in the transition region. The second degree of crystallization happens when the mixture contains a few crystals. The third degree of crystallization happens when the mixture has a slushy consistency. Many crystals form in the mixture, but the mixture is still mostly liquid. The fourth degree of crystallization is the last one in the transition region and occurs when the mixture is roughly half crystals and half liquid. The final region is complete crystallization of the mixture. Mixtures in this region are mostly crystals, and at the extreme end of

100% FHIL they are completely crystallized solids.

(a) Degree 1. (b) Degree 2. (c) Degree 3. (d) Degree 4. (e) Degree 5.

Figure 2-2: Degrees of crystallization
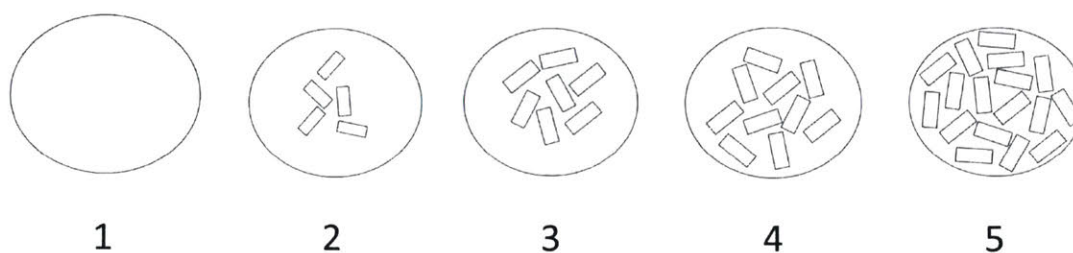
Figure 2-3: Artistic impression of the degrees of crystallization.

Mixtures of EMI-$(HF)_{2.3}$F with EMI-CF_3BF_3 remain liquid below concentrations of 56-60% EMI-$(HF)_{2.3}$F by mass. A line plot of the crystallization transition for EMI-$(HF)_{2.3}$F is shown below in Figure 2-4. The numbers 1–5 correspond to the degrees of crystallization shown in Figures 2-2 and 2-3.
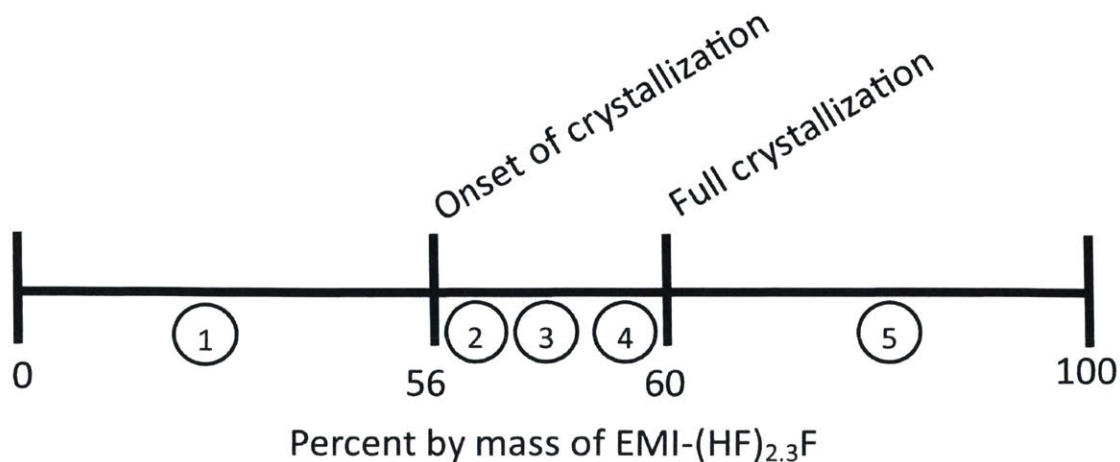
Figure 2-4: Crystallization transition for the FHIL EMI-$(HF)_{2.3}$F.

21

The same crystallization phenomenon occurs in S_{111}-$(HF)_{1.9}F$. The crystallization transition region occurs at 62-66% S_{111}-$(HF)_{1.9}F$. Figure 2-5 shows the line plot for the crystallization of S_{111}-$(HF)_{1.9}F$. S_{111}-$(HF)_{1.9}F$ crystallizes at a higher concentration
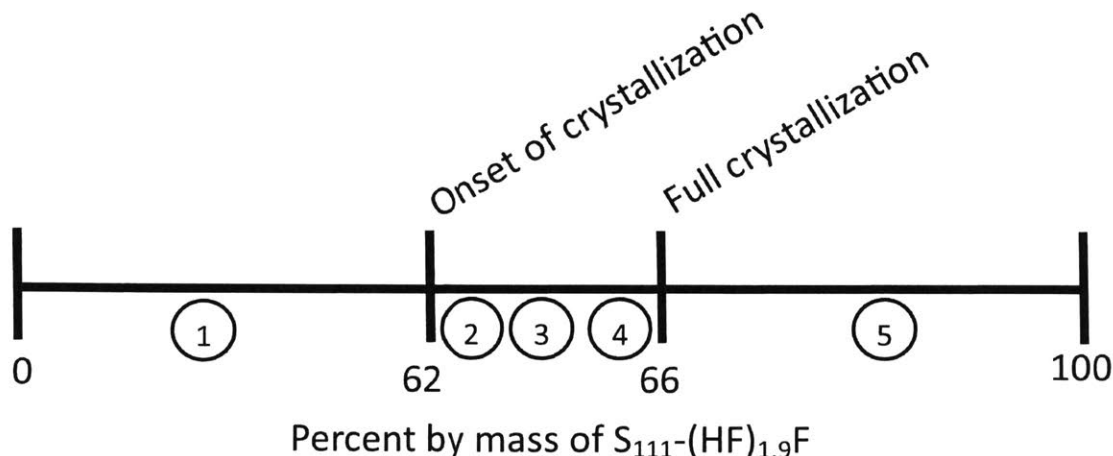
Figure 2-5: Crystallization transition for the FHIL S_{111}-$(HF)_{1.9}F$.

than EMI-$(HF)_{2.3}F$. This should allow for mixtures with higher concentrations of the FHIL, and therefore increased emitted current.

2.2   Relative Electrical Conductivites of Mixtures

Once the crystallization boundaries of the two FHILs were determined, three concentrations of each FHIL were chosen for future experiments. For both EMI-$(HF)_{2.3}F$ and S_{111}-$(HF)_{1.9}F$, concentrations of 10%, 25%, and 50% were investigated. All of these concentrations are below 56% FHIL, which is the boundary where EMI-$(HF)_{2.3}F$ begins to crystallize. Although S_{111}-$(HF)_{1.9}F$ has a higher crystallization boundary, the same concentrations of both FHILs were chosen for comparison purposes between the FHILs.

For each of these concentrations, the relative conductivity of the mixtures at room temperature were determined using the conductivity of EMI-CF_3BF_3 as the baseline. The relative conductivity of each mixture was determined by measuring the resistance through the mixture. A thin capillary was filled with a mixture. Platinum wire was

inserted into each end of the capillary, and an ohmmeter was used to determine the resistance through the mixture. The platinum wire was inserted approximately the same distance inside the capillary for all the mixtures. Resistance and conductivity are inversely related in the equation $K = \frac{4}{R}\frac{L}{\pi D^2}$, so the relative conductivity of each mixture was determined by dividing the resistance of the mixture by the resistance of the pure EMI-CF$_3$BF$_3$.

The results of the relative conductivity test are summarized in Table 2.1. These

Table 2.1: Relative Conductivities of FHIL Mixtures with EMI-CF$_3$BF$_3$

FHIL Concentration	Relative Conductivity
0% FHIL (100% EMI-CF$_3$BF$_3$)	1
10% EMI-(HF)$_{2.3}$F	1.8
25% EMI-(HF)$_{2.3}$F	3.7
50% EMI-(HF)$_{2.3}$F	5.5
10% S$_{111}$-(HF)$_{1.9}$F	1.8
25% S$_{111}$-(HF)$_{1.9}$F	2.3
50% S$_{111}$-(HF)$_{1.9}$F	3.4

results show a general pattern of increased conductivity as the mass fraction of FHIL increases. Although S$_{111}$-(HF)$_{1.9}$F has a higher conductivity than EMI-(HF)$_{2.3}$F, the EMI-(HF)$_{2.3}$F mixtures have a higher relative conductivity for the same mass fraction of FHIL. This is an interesting, unexplained result. Future work should probe the possible reasons for this apparent contradiction of expectations. It is also possible that the result is due to measurement error, which was not estimated in these measurements, or to procedural error. Additional conductivity measurements are underway, and results will be reported in the future.

2.3 Time of Flight

The final experiment was the characterization of how each mixture behaved when fired from a single carbon xerogel emitter. Current-voltage (I-V) curves and time of flight (TOF) tests were used to characterize the performance of each FHIL mixture.

TOF spectrometry is used to determine the composition of the emitted ion beam. The setup, a diagram of which is shown in Figure 2-6, consists of a deflector gate and a channeltron which collects the emitted beam. The deflector gate is turned on and off. When the gate is on, charged particles are deflected away from the channeltron. When the gate is off, charged particles are allowed to flow to the channeltron, where they are collected. The lighter ions arrive at the channeltron first, followed by the heavier ions and droplets. From the current received by the channeltron over time, it can be determined which charged species are in the beam and what percentage of the beam is composed of monomers, heavier ions such as dimers and trimers, or other species, like charged droplets [15].
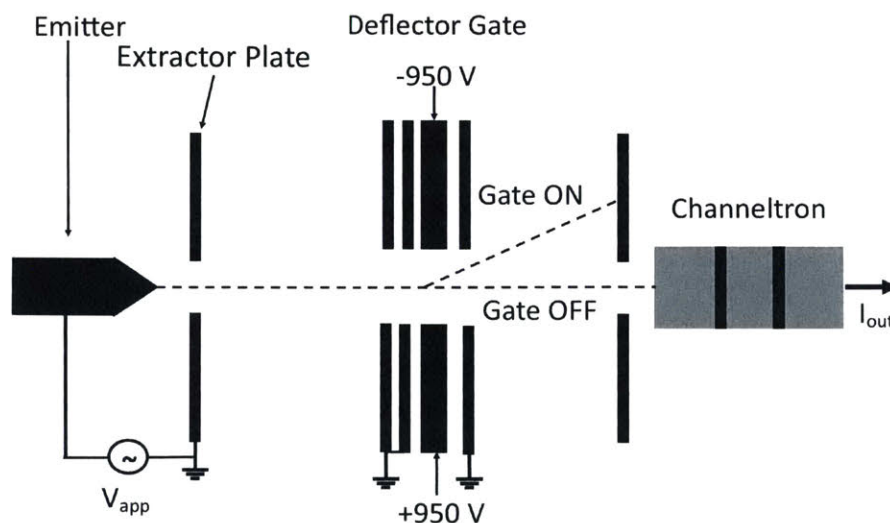
Figure 2-6: TOF setup, adapted from Ref. [15] and [10].

Preparation of the TOF setup requires multiple steps. First, the emitter must be fabricated. The emitters used in this experiment were made of resorcinol formaldehyde carbon xerogel. This material was made by mixing a solution of resorcinol, formaldehyde, acetone, and water. This solution was then poured into cylindrical spaces in a mold. Into each cylindrical space, a 1 mm diameter stainless steel rod was inserted. This rod was used later in the process to hold the carbon xerogel cylinder while sharpening the emitter tip. The mold was placed into a closed container to set for 24 hours. After 24 hours, the container was placed in an oven to cure for four

days. Over the course of the four days, the temperature of the oven was increased from 40°C to 80°C. Then the container was taken out of the oven and its lid removed, permitting the resorcinol formaldehyde emitters to dry, and the container and the mold then sat in the fume hood for 24 hours. After 24 hours, the open container holding the mold was then placed back into the 80°C oven for a final 48 hours [10].

After the final 48 hours, the container was removed from the oven and the mold was allowed to cool. Once the mold cooled, the solid resorcinol formaldehyde emitters were removed from the mold. The emitters were then sharpened into a cone with a half-angle of $\sim 10°$ using a Dremel tool and sandpaper. The stainless steel rod in the emitter was held by the Dremel, and the Dremel spun the emitter, sharpening the other end on the sandpaper. After the carbon xerogel emitters were sharpened, they were pyrolized in a 900°C tube furnace for four hours while 400 sccm argon gas flowed over them. Once an emitter tip was pyrolized it was ready for use. The emitters used in this experiment were created by Dr Perez-Martinez. Further details on how the emitters were sharpened can be found in Ref. [10].

After the tip was pyrolized, most of the stainless steel rod was cut off. The emitter was then wrapped with HF-compatible filter paper and a platinum wire was wrapped around the filter paper to secure it. The platinum wire was also later used to connect the emitter with the high voltage source. The emitter, filter paper, and platinum wire were then placed in a porous Teflon cylinder. The Teflon cylinder was then set into the TOF test stand. Next, the end of the platinum wire was wrapped around a set screw. A nut secured the platinum wire, followed by another wire which connected to the high voltage source and was secured with another nut on the set screw. The assembly process is shown in Figure 2-7.

Finally, the extractor plate was placed on the test stand above the emitter and the emitter tip was centered on the hole in the extractor plate. The final setup is shown in Figure 2-8. The test stand was then attached to the flange of the vacuum chamber, and the vacuum chamber was sealed and pumped down to below 1×10^{-5} Torr.

TOF testing was run using an oscilloscope. The voltage across the deflection

(a) Carbon xerogel emitter.

(b) Emitter with filter paper.

(c) Wrapped with platinum wire.

(d) In teflon cylinder.
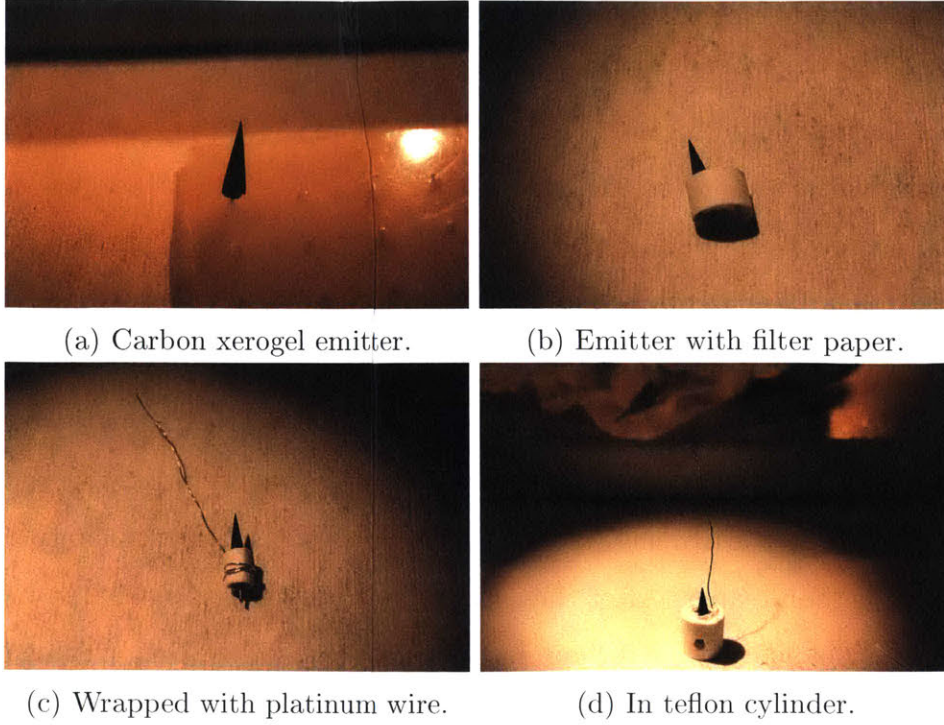
Figure 2-7: Emitter assembly.

(a) Angled view of TOF test stand.

(b) Side veiw of TOF test stand.
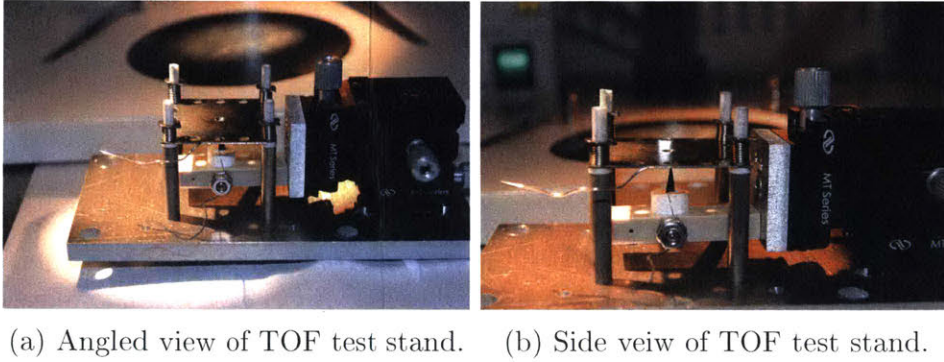
Figure 2-8: TOF test stand.

gate electrodes was 1900 V. Further details of the TOF test setup can be found in Ref [15]. TOF experiments were done for mixtures of both EMI-$(HF)_{2.3}$F and S_{111}-$(HF)_{1.9}$F at concentrations of 10%, 25%, and 50%. For each mixture, TOF data was recorded on the oscilloscope for a 200-300 V range of applied voltages in the positive mode with intervals of 50 V. Five to ten sets of TOF data were taken for each FHIL mixture. Due to the difficulty of fabricating emitters with sufficiently sharp tips, two were used to conduct all of the TOF experiments. In between testing different

mixtures, the emitter was cleaned in sonic baths of isopropanol and acetone and the tip hand-sharpened on a small piece of 2500-grit sandpaper. However, the reuse and hand-sharpening resulted in emitter tips that became less sharp over time.

Ideally, electrospray thrusters should operate in the pure ionic regime (PIR), meaning the charged particle beam is completely composed of ions without the presence of droplets. Within the PIR a beam composed solely of monomers is beneficial. A beam composed solely of monomers maximizes I_{sp}, because it contains only the fastest, lightest-weight charged species. In cases where the beam contains only one species of ion, this beam will also be more efficient, because there will be no polydispersity and all the ions will be accelerated to the same velocity. All six mixtures operated in the PIR, with beams composed only of monomers and dimers. Table 2.2 summarizes the results of the TOF testing. Pure EMI-CF$_3$BF$_3$ was used as a baseline for comparison against the FHIL mixtures. Pure EMI-CF$_3$BF$_3$ is roughly 50% EMI+

Table 2.2: TOF Results

Mixture	Monomer	Dimer
EMI-CF$_3$BF$_3$	50% EMI+	50% (EMI-CF$_3$BF$_3$)-EMI+
10% EMI-(HF)$_{2.3}$F	59% EMI+	41% (EMI-CF$_3$BF$_3$)-EMI+
25% EMI-(HF)$_{2.3}$F	76% EMI+	24% (EMI-CF$_3$BF$_3$)-EMI+
50% EMI-(HF)$_{2.3}$F	51% EMI+	25% (EMI-(HF)$_{2.3}$F)-EMI+ 24% (EMI-CF$_3$BF$_3$)-EMI+
10% S$_{111}$-(HF)$_{1.9}$F	55% EMI+	45% (EMI-CF$_3$BF$_3$)-EMI+
25% S$_{111}$-(HF)$_{1.9}$F	15% S$_{111}$+ 85% EMI+	no dimers detected
50% S$_{111}$-(HF)$_{1.9}$F	39% EMI+	61% (S$_{111}$-(HF)$_{1.9}$F)-S$_{111}$+

ions (monomers), and 50% (EMI-CF$_3$BF$_3$)-EMI+ dimers. As the amount of FHIL in the mixture was increased, the percent of monomers increased and dimers were sup-

pressed. However, past a certain point, adding FHIL did not increase the percentage of monomers in the beam. Instead, for both EMI-$(HF)_{2.3}F$ and S_{111}-$(HF)_{1.9}F$ the mixtures of 50% FHIL had a lower percentage of monomers than the 25% FHIL mixtures. Figure 2-9 shows the TOF results for the EMI-$(HF)_{2.3}F$ mixtures. The presence of
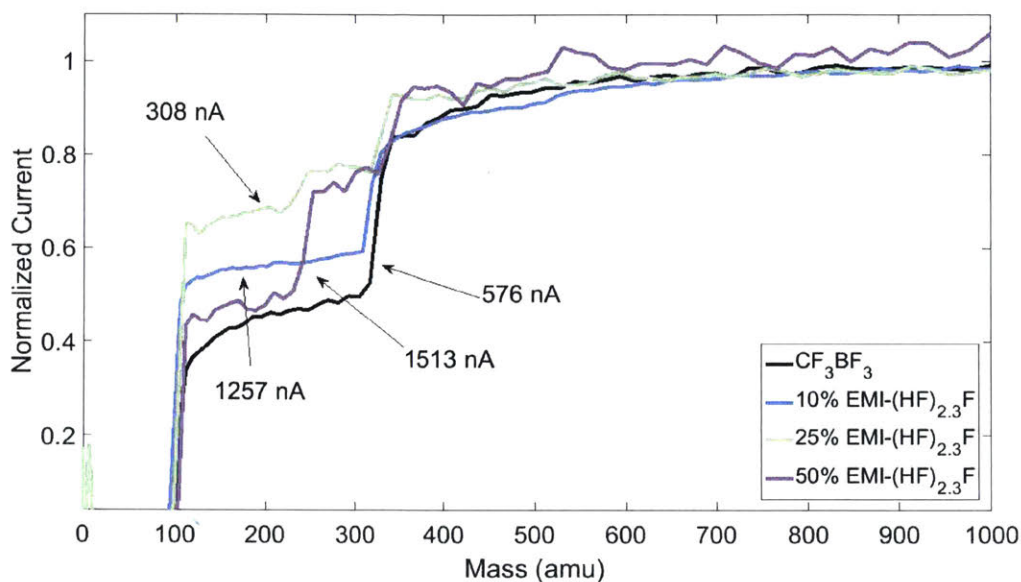

Figure 2-9: TOF results for EMI-$(HF)_{2.3}F$.

EMI-$(HF)_{2.3}F$ suppressed some of the emission of dimers, but not all. The 50% EMI-$(HF)_{2.3}F$ mixture contained both (EMI-CF_3BF_3)-EMI+ and (EMI-$(HF)_{2.3}F$)-EMI+ dimers, while in the other mixtures only (EMI-CF_3BF_3)-EMI+ was present. The optimum mixture for EMI-$(HF)_{2.3}F$ in which all dimers and larger charged particles are suppressed probably occurs between 25% and 50% EMI-$(HF)_{2.3}F$. Further testing should be conducted to find this optimum.

I-V curves were also performed for all the mixtures. Figure 2-10 compares the results for the EMI-$(HF)_{2.3}F$ mixtures against pure EMI-CF_3BF_3. The 10% EMI-$(HF)_{2.3}F$ performed the best. However, this is most likely due to the order of testing. The 10% EMI-$(HF)_{2.3}F$ mixture was the first mixture to be tested. The emitter tip was therefore very sharp and unused. This explains why the 10% EMI-$(HF)_{2.3}F$ produced more current at lower voltages. Further experiments should be conducted with separate, identical emitters for each FHIL mixture in order to obtain a more
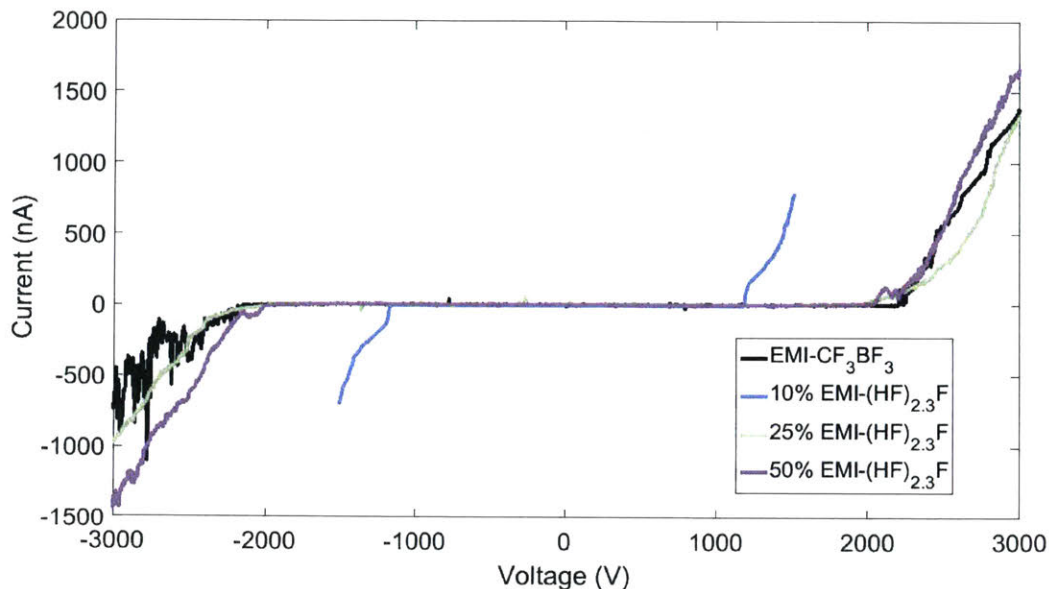
accurate comparison between the mixtures.

Figure 2-10: I-V curves for EMI-$(HF)_{2.3}F$.

For S_{111}-$(HF)_{1.9}F$, the optimum mixture for I_{sp} is 25% S_{111}-$(HF)_{1.9}F$. In this mixture, the beam is entirely monomers. While all the S_{111}-$(HF)_{1.9}F$ beams contained EMI+, the 25% S_{111}-$(HF)_{1.9}F$ beam also contained S_{111}+ monomers, which comprised 15% of the beam. The 50% S_{111}-$(HF)_{1.9}F$ beam contained the lowest percentage of EMI+ monomers, and also contained $(S_{111}$-$(HF)_{1.9}F)$-S_{111}+ dimers. Figure 2-11 shows the TOF results for the S_{111}-$(HF)_{1.9}F$ mixtures.

Not only did the 25% S_{111}-$(HF)_{1.9}F$ mixture beam produce only monomers, but this mixture also produced the most current. Similar to the EMI-$(HF)_{2.3}F$ mixtures, the significantly higher current produced by the 25% S_{111}-$(HF)_{1.9}F$ mixture might be caused in part by a sharper tip. However, this mixture was the last mixture to be tested, after the emitter had been hand-sharpened many times. The 10% and 50% S_{111}-$(HF)_{1.9}F$ mixtures performed better than the EMI-CF_3BF_3 baseline, but did not show significantly increased current like the 25% S_{111}-$(HF)_{1.9}F$. The I-V curves for the S_{111}-$(HF)_{1.9}F$ mixtures are shown in Figure 2-12.

Despite the degradation of the emitters over time due to using the same emitters
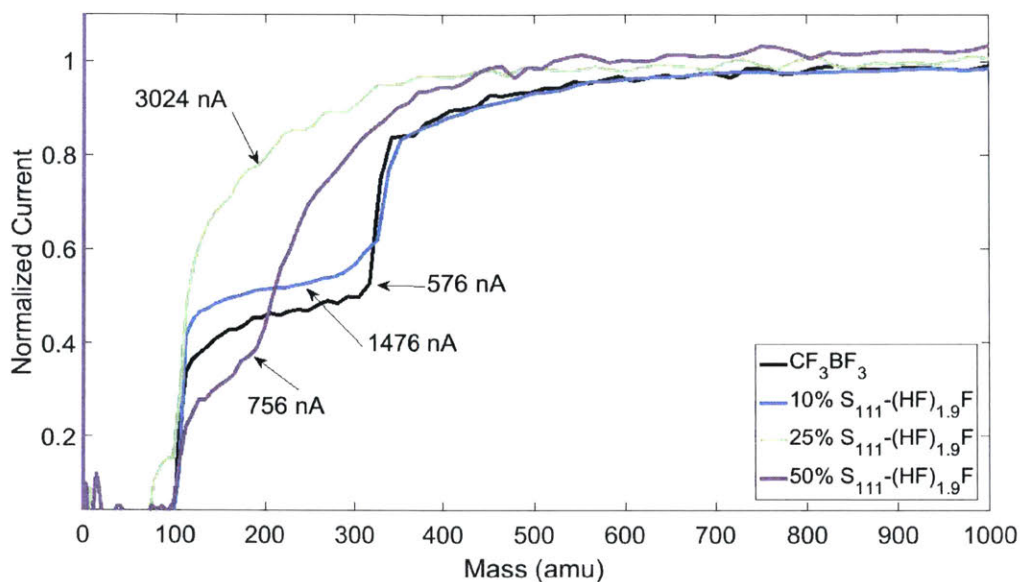
Figure 2-11: TOF results for S_{111}-$(HF)_{1.9}F$.
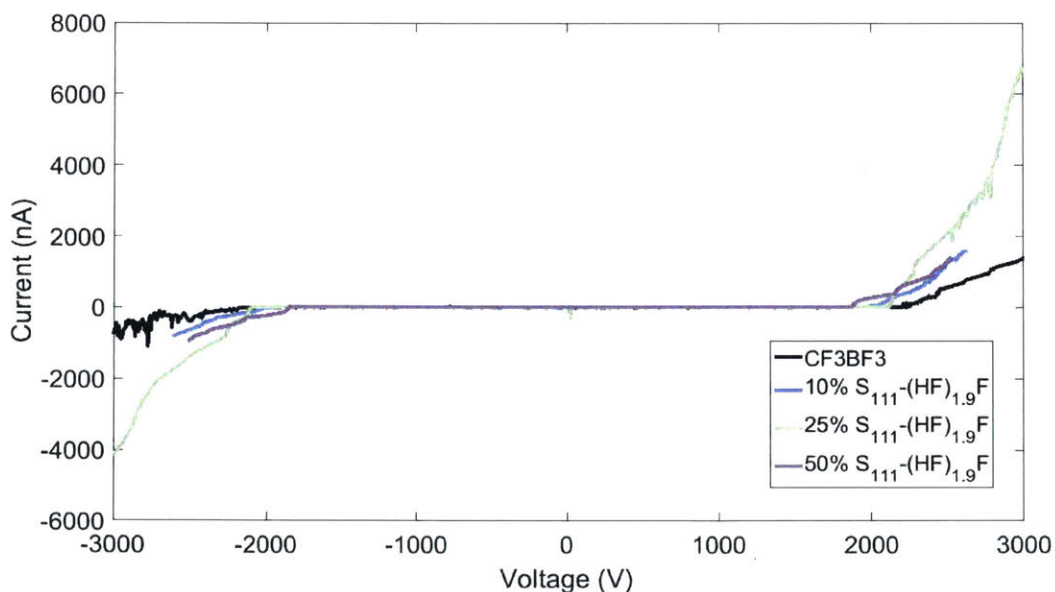
Figure 2-12: I-V curves for S_{111}-$(HF)_{1.9}F$.

to test multiple mixtures, the data shows a clear improvement by adding FHILs to EMI-CF_3BF_3. The EMI-$(HF)_{2.3}F$ mixtures all showed an increase in the percentage of monomers in the beam over the EMI-CF_3BF_3 baseline. All three S_{111}-$(HF)_{1.9}F$ mixtures showed an increase in current over EMI-CF_3BF_3. All six FHIL mixtures operated in the PIR, producing only monomers and dimers. The TOF and I-V data

30

presented above suggests that there is an optimum mixture ratio for the FHILs that optimizes current and the presence of monomers in the beam. However, this should be investigated in future work in which a different emitter is used for each FHIL mixture. Different mass fractions of FHILs produced varying degrees of clustering in the beam. In the case of 25% S_{111}-$(HF)_{1.9}F$, the mixture produced both high current and a beam composed solely of monomers.

The TOF data was then used to determine the average charge-to-mass ratios for the 25% S_{111}-$(HF)_{1.9}F$ and 50% S_{111}-$(HF)_{1.9}F$ mixtures and calculate the performance characteristics I_{sp} and thrust for each. These mixtures have the highest percentage of monomers or dimers, respectively, and therefore represent the upper and lower bounds of the performance of the FHIL mixtures. Both I_{sp} and thrust in electrospray thrusters are dependent on the voltage to the extractor plate. I_{sp} is calculated using the equation $I_{sp} = \frac{1}{g}\sqrt{2\frac{q}{m}V}$, where $\frac{q}{m}$ is the average charge-to-mass of the charged particles in the beam and V is the voltage. The force of thrust is calculated using the equation $F = I\sqrt{\frac{2V}{q/m}}$. In the TOF experiments, voltages up to 3,000 V were applied to the extractor plate. However, for iEPS, operational voltages range between 700 V and 2000 V.

In Figure 2-13 voltage versus I_{sp} is plotted for the baseline EMI-CF_3BF_3, 25% S_{111}-$(HF)_{1.9}F$, and 50% S_{111}-$(HF)_{1.9}F$ for the range of voltages used in iEPS. While the 50% S_{111}-$(HF)_{1.9}F$ mixture had a lower percentage of monomers than the EMI-CF_3BF_3 baseline did, the presence of the lighter $(S_{111}$-$(HF)_{1.9}F)$-$S_{111}+$ dimer in the beam lowered the average mass of the charged particles in the beam. The lower average masses in the 25% S_{111}-$(HF)_{1.9}F$ and 50% S_{111}-$(HF)_{1.9}F$ mixtures resulted in higher I_{sp} than for EMI-CF_3BF_3 for the same voltages. At 2,000 V, the 25% S_{111}-$(HF)_{1.9}F$ mixture had an I_{sp} 2,000 s higher than EMI-CF_3BF_3 did.

The other important performance characteristic is thrust. The calculated thrust curves for 25% and 50% S_{111}-$(HF)_{1.9}F$ are shown in Figure 2-14. For these calculations, the same voltage range was used, and current was varied between 0.5 μA and 2μA. Because thrust is inversely proportional to the square of the charge-to-mass
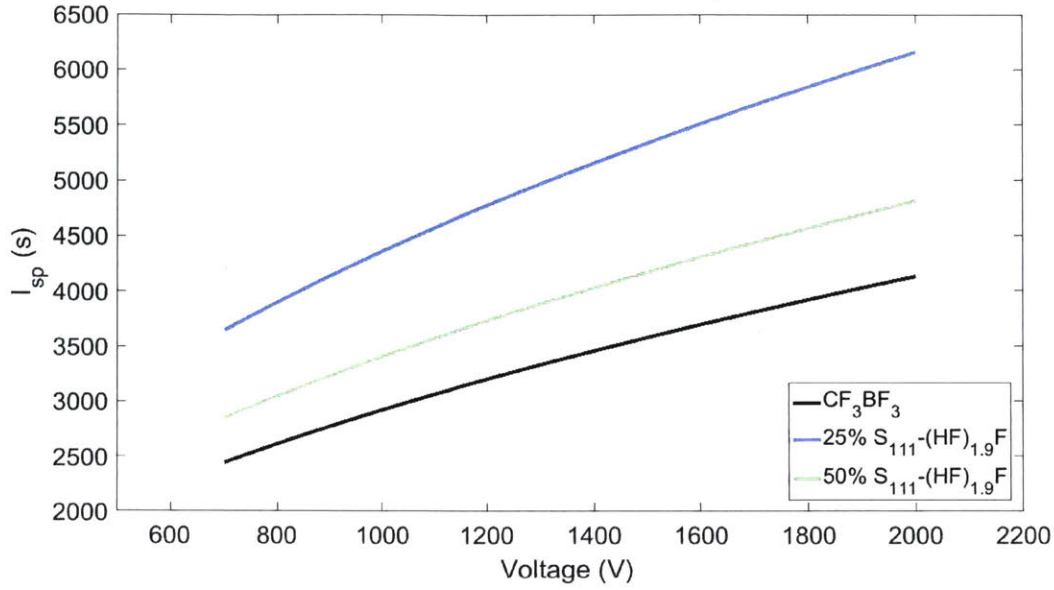
31

Figure 2-13: I_{sp} bounds for FHIL mixtures.

ratio and the 50% S_{111}-$(HF)_{1.9}F$ mixture had a higher average mass, this mixture produced higher thrust for the same voltage and current. If the thrust for EMI-CF_3BF_3 were plotted, it would show even higher thrust for the same current, because the EMI-CF_3BF_3 beam had an even higher average mass. However, in the above TOF experiments, the 25% S_{111}-$(HF)_{1.9}F$ mixture produced significantly higher current than EMI-CF_3BF_3 and the other S_{111}-$(HF)_{1.9}F$ mixtures for the same voltages, up to an almost five-fold increase over EMI-CF_3BF_3. Therefore, when the same voltage is applied, the current produced by the 25% S_{111}-$(HF)_{1.9}F$ mixture should increase, producing higher thrust than EMI-CF_3BF_3.
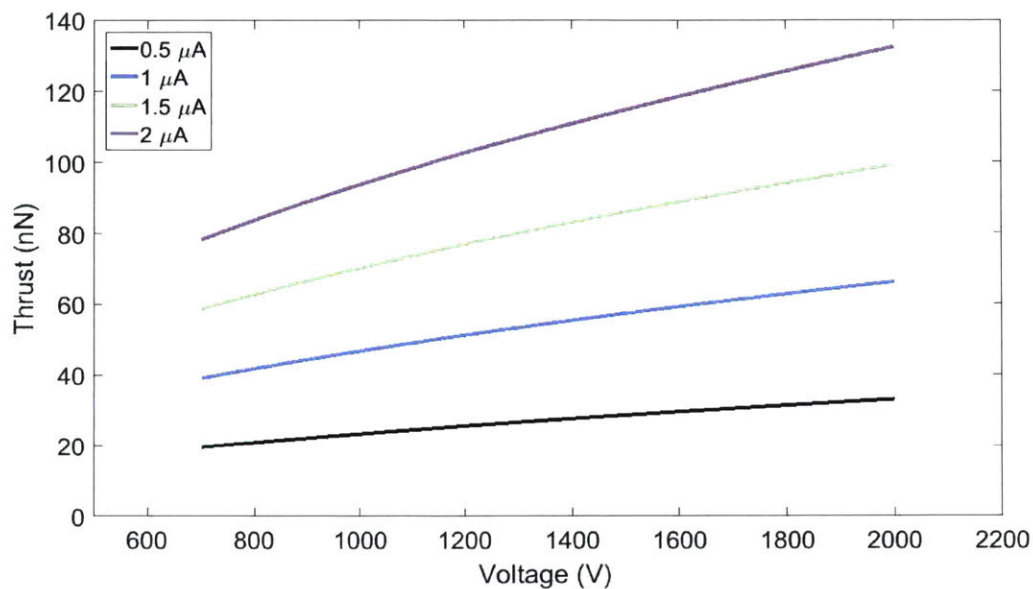
(a) Thrust curves for 25% S_{111}-$(HF)_{1.9}F$.
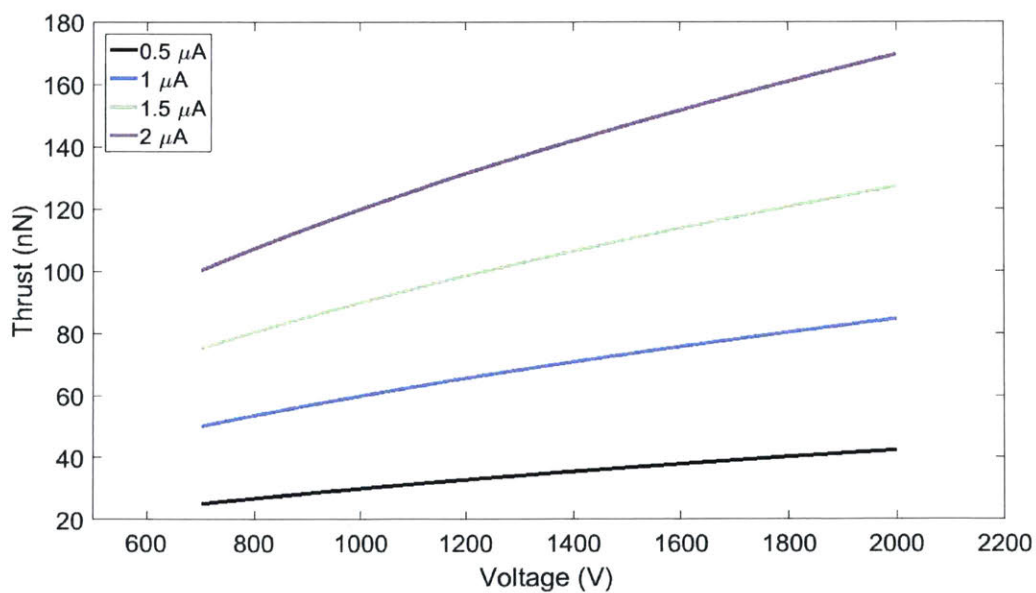
(b) Thrust curves for 50% S_{111}-$(HF)_{1.9}F$.

Figure 2-14: Thrust curves for 25% and 50% S_{111}-$(HF)_{1.9}F$.

Chapter 3

Conclusion

FHILs are a promising method for increasing the thrust density of iEPS. However, because $EMI\text{-}(HF)_{2.3}F$ and $S_{111}\text{-}(HF)_{1.9}F$ crystallize in vacuum, it was necessary to investigate mixtures of these FHILs with $EMI\text{-}CF_3BF_3$. The first experiment in this thesis determined the crystallization transition region of the two FHILs. For $EMI\text{-}(HF)_{2.3}F$, this transition occurred from 56% to 60% concentration by mass, and for $S_{111}\text{-}(HF)_{1.9}F$ the transition occurred between 62% and 66%. Once the crystallization transition regions of the two FHILs were found, varying concentrations of the FHILs below their crystallization boundaries were investigated using TOF to determine their beam compositions. For both FHILs, concentrations of 10%, 25%, and 50% were investigated. The TOF results showed that all six FHIL mixtures operated in the PIR. The 25% $S_{111}\text{-}(HF)_{1.9}F$ mixture was unique in that it produced only monomers. Within the range of voltages used for iEPS, this mixture had an improvement in I_{sp} up to 2,000 s over $EMI\text{-}CF_3BF_3$. For the same current and voltage, the 25% $S_{111}\text{-}(HF)_{1.9}F$ mixture had lower average mass than $EMI\text{-}CF_3BF_3$. However, since the 25% $S_{111}\text{-}(HF)_{1.9}F$ produced much higher current density, it should ultimately produce more thrust than $EMI\text{-}CF_3BF_3$ for a given applied voltage.

This research demonstrates that FHILs are a good additive to $EMI\text{-}CF_3BF_3$ for use as iEPS propellant, in particular the 25% $S_{111}\text{-}(HF)_{1.9}F$ mixture. It produced a significantly higher current than the baseline $EMI\text{-}CF_3BF_3$ did and emitted a beam composed exclusively of monomers, leading to higher I_{sp}. It also has the benefit of

being well below the crystallization transition region for S_{111}-$(HF)_{1.9}F$.

This work also raises important questions to be answered by future research. While I believe the trends in my TOF and I-V measurments to be accurate, repeating them with a new carbon xerogel emitter for each mixture will increase the precision of the measurement and increase confidence in the result. Additional research should also be conducted to determine if EMI-$(HF)_{2.3}F$ has an optimum mass fraction that maximizes the emission of monomers, greatly increases the produced current, or both. Future TOF work could also include investigating S_{111}-$(HF)_{1.9}F$ mixtures around 25% for a more precise value of the optimum mass fraction. The reasons for EMI-$(HF)_{2.3}F$ mixtures demonstrating higher relative conductivity than S_{111}-$(HF)_{1.9}F$ mixtures should be investigated, as they may shed new light on the use of FHIL mixtures and hint at optimizations to be made. Such investigations could begin with repeated conductivity measurements to establish statistical error bounds on the results. Finally, research should also be conducted into what causes the crystallization of the pure FHILs and mixtures containing high percentages of FHIL.

Appendix A

Lincoln Laboratory Research: WaferSat

A.1 Introduction

WaferSat is a new type of miniature satellite being developed at MIT Lincoln Laboratory, constructed on silicon wafers. The WaferSat bus will be cheap to produce in bulk, at an expected price point of $15,000 per satellite, allowing end users to put tens, hundreds, or even thousands of them into space for less than the cost of a larger satellite, which can easily exceed $1 billion. Possible missions for WaferSat constellations include investigation of the Earth's ionosphere and synthetic large aperture imagery. Like most satellites, but unlike many other minature satellites, WaferSats will have an on-board propulsion system. This propulsion system is modeled after the iEPS from MIT SPL.

Since WaferSats have an unusal combination of size, mass, and shape, a study of their motion is necessary. This study, conducted in MATLAB, was a general first pass at understanding how a WaferSat will move in space. It assumed a 2-D frictionless plane, point thrusters, and no external forces (such as gravity or drag), in order to provide a basic understanding of how an individual WaferSat will move within its orbit. The process of developing the simulator began with describing the basic translational and rotational motion of a WaferSat when subjected to the force

from a single thruster. Next, combinations of thruster firings were added to the simulation to allow for more complex maneuvering. After that, thruster position offset was investigated to determine the WaferSat's sensitivity to misalignment of thrusters. Finally, a genetic algorithm was investigated for its future use in creating firing command sequences to move the WaferSat to a desired location.

A.1.1 Background

The space community has been interested in the idea of a "satellite-on-a-chip" since at least 1994, when the idea was first proposed [16, 17]. In 1999, Janson of Aerospace Corp. proposed a batch-produced, "system-on-a chip" satellite made of silicon[18]. The proposed satellite, shown in Figure A-1, was a thick cylindrical "stacked multi-wafer system", the dimensions of which were 10 - 30 cm.
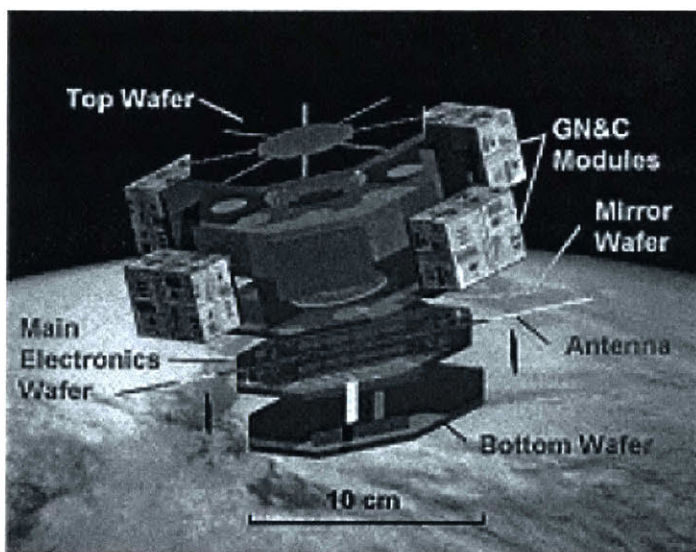
Figure A-1: Aerospace Corp silicon satellite, from Ref. [18].

This proposed satellite included a propulsion system to facilitate the control of clusters and constellations of the satellites. One proposed propulsion system concept was digital micropropulsion, an array of single-shot thrusters. Each of these single-shot thrusters would be a microcavity containing propellant and an ignitor, and would be individually sealed and controllable. Thousands of microthrusters would allow the spacecraft to perform hundreds of maneuvers in orbit. A major drawback of

this design is the one-time use of each microthruster. If the spacecraft fired all of the microthrusters in one location, it would be unable to perform future maneuvers. Janson also briefly proposed a microfabricated resistojet (a type of electric propulsion that operates by heating propellant and then expanding it through a traditional nozzle) as the propulsion system instead [18]. However, as the size of a resistojet is decreased, so too is its efficiency. Aerospace Corp never fabricated any of this silicon wafer-based satellite.

In the same year that Janson proposed his silicon spacecraft, the Surrey Space Centre in the UK set a goal to build a "satellite-on-a-chip" [16]. This would be a true stand-alone system-on-a-chip, as opposed to a stack of silicon wafers. The system-on-a-chip design was attractive, because of its potential mass producibility and low cost per unit. These same benefits are also drivers behind MIT Lincoln Laboratory's current WaferSat project. The Surrey Space Centre developed a prototype, named "PCBSat", which was a 70 g satellite-on-a-PCB, shown in Figure A-2. Although the prototype PCBSat was fabricated, none were ever launched.
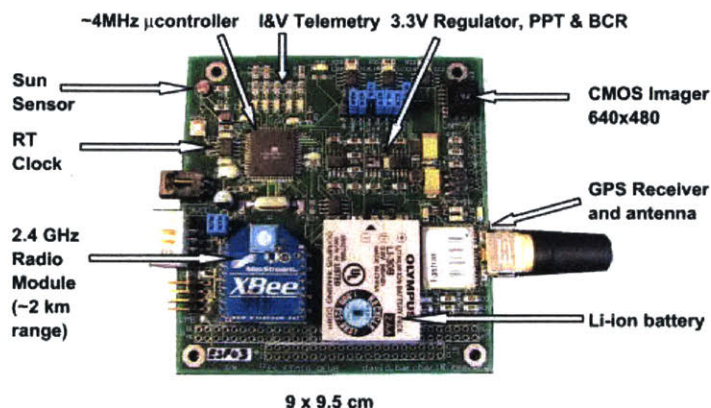
Figure A-2: PCBSat, from Ref. [19].

Surrey Space Centre's conceptual design, SpaceChip, shown in Figure A-3, was to be the first monolithic satellite-on-a-chip. It was proposed as a solution for distributed missions, such as distributed aperture radar, that require a large number of nodes. A generic mission design would include a large number of SpaceChips which would be deployed from a mothership in low Earth orbit (LEO). The mothership would
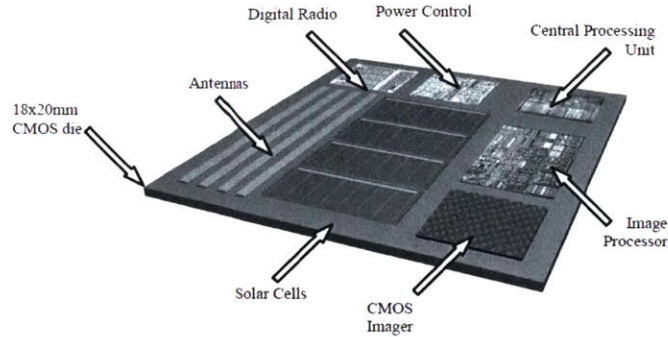
Figure A-3: SpaceChip, from Ref. [16].

then relay information between the cluster of SpaceChips and the ground station. The SpaceChip bus would have many of the same subsystems as larger spacecraft, including structural, electrical power, data handling, and communication subsystems. Notably, SpaceChip would not have a propulsion subsystem. This lack of a propulsion subsystem combined with atmospheric drag would result in a short operating life for the SpaceChip cluster. The design of SpaceChip included a maximum circuit area of 360 mm^2 and a maximum mass of less than 10 g [16]. No SpaceChips were ever fabricated or launched.

The next proposal for tiny, inexpensive satellites was the Silicon Wafer Integrated Femtosatellite (SWIFT) developed by Chung and Hadaegh at NASA's Jet Propulsion Laboratory (JPL). The goal of this project was to be able to create a distributed aperture array composed of a swarm of "fully capable femtosats" [20]. Chung and Hadaegh defined "femtosat" as the 100 g class of spacecraft. Each satellite would be manufactured using "3-D silicon wafer fabrication and integration techniques" and would be actively controlled in all six degrees of freedom [20]. JPL developed several key subsystem requirements for the SWIFT spacecraft. These included an I$_{sp}$ of greater than 100 s, and a ΔV of 24 m/s for a three-month mission [21]. SWIFT would therefore need a propulsion subsystem. Two notional designs, shown in Figure A-4, include either a digital microthruster system, similar to the propulsion subsystem proposed by Janson for his satellite, or a miniaturized warm gas hydrazine system. Hadaegh, Chung, and Manohara also proposed electrospray thrusters for the propulsion subsystem, which would use either indium or ionic liquid propellant [21]. The
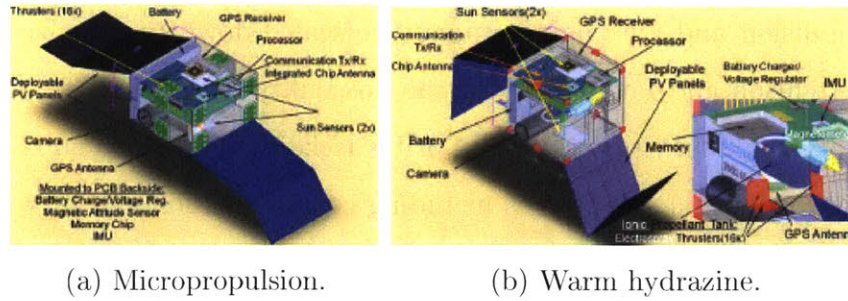
40

(a) Micropropulsion. (b) Warm hydrazine.

Figure A-4: Two notional designs of SWIFT, from Ref. [21].

total mass of the propulsion subsystem was required to be less 40 g. However, they had difficulty meeting this mass requirement, stating that the "development of a fully capable 100-g-class femtosat hinges on ...the successful miniaturization of the propulsion system" [21]. The SWIFT propulsion system would require two thrust levels: a high thrust of approximately 100 µN to position the spacecraft in orbit and a low thrust of approximately 10 µN for station-keeping. On the larger, satellite-wide scale, Hadaegh, Chung, and Manohara decided to design SWIFT using primarily chip-level integration, rather than the wafer-scale integration they originally proposed. Wafer scale integration was proposed instead for occasional use in manufacturing the femtosats. Initially wafer scale integration was proposed because it would result in a low-power spacecraft, but it was less modular and more expensive than chip-level integration. No SWIFT spacecraft were ever produced [21].

The final "satellite-on-a-chip" precursor to WaferSat was the Sprite satellite developed at Cornell University [22]. Sprites were 3.5 cm by 3.5 cm satellites weighing 5 g. A flight model is shown in Figure A-5. They did not have a propulsion subsystem.
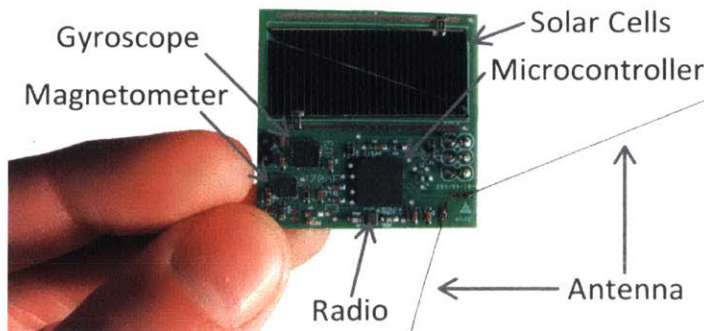

Figure A-5: Sprite flight model, from Ref. [22].

Chemical propulsion and ion engines cannot be scaled down to the size needed for Sprites, but Atchison and Peck proposed the possibility of adding digital propulsion to future iterations of the Sprite. While Sprites lacked a propulsion subsystem, they did have other traditional subsystems including communication and power [23]. The basic mission for Sprites involved a mothership called KickSat from which 128 Sprites would deploy. Sprites were expected to spend only a few days in orbit before reentering Earth's atmosphere [22]. KickSat and 128 Sprites were launched in April 2014; however, the Sprites were not able to deploy from the KickSat mothership before it deorbited [24].

WaferSat shares many similariteis with its predecessors. It is designed to be a low-cost, mass-producible satellite bus, which can be used for many types of missions including distributed aperture radar, space weather monitoring, and communication relays. Like SWIFT and the system-on-a-chip design proposed by Janson, WaferSat will have a propulsion system. However, this propulsion system will be an electrospray propulsion system based on the iEPS developed at MIT SPL. Unlike in the previous spacecraft designs, the WaferSat structure will be a bonded stack of a few 200 mm diameter silicon wafers [25]. It will be smaller than Janson's satellite and SWIFT, but large enough for a propulsion sytem, and have a unique disk shape.

A.2 Research

A.2.1 WaferSat Motion

WaferSats have the potential to be used for a variety of missions. However, they have a unique shape for satellites, and the effect of the disk shape on orbital motion must be investigated. The simplest orbit for a satellite is a circular orbit with a semi-major axis $a = R_e + $ alt, where R_e is the mean radius of the earth, 6378 km, and alt is the satellite's altitude. In this study, the motion of a WaferSat was constrained to a few kilometers. The space the WaferSat was operating in was much smaller than the semi-major axis of its orbit. Therefore, for the purpose of this study, the WaferSat

was assumed to move in a 2-D x–y plane. To further simplify the problem, the plane was frictionless and external forces such as gravity and drag were ignored.

WaferSat has a radius of 0.1 m, and for the purpose of this study had a mass of 50 g. This mass is on the low end of the projected range of masses for the WaferSat bus. WaferSat will have two types of thrusters: in-plane and out-of-plane. In-plane thrusters will be used for orbit changing and station-keeping, and in this study the thrusters controlled the WaferSat's motion in the $x - y$ plane. Out-of-plane thrusters will provide attitidue control by providing rotation about the WaferSat's $x-$ and $y-$axes. This study focused on the in-plane thrusters while the out-of-plane thrusters were ignored. The WaferSat was assumed to have a center of mass located at its geometric center. Four iEPS-style thrusters were directed radially in the $+x$, $+y$, $-x$, and $-y$ directions, as shown in Figure A-6. The thrusters were assumed to each provide 15 µN of thrust and act on a single point on the body of the WaferSat. For the purpose of this simulation, the thrusters fired at full thrust or were turned off.
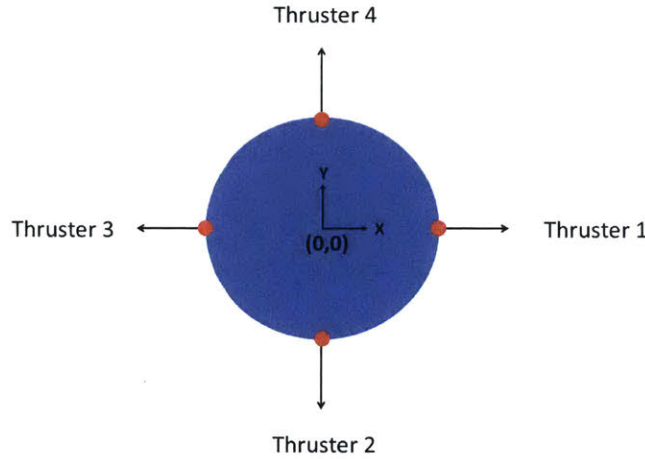
Figure A-6: WaferSat with purely radial thruters.

The motion of the WaferSat was described using the basic equations for translational and rotational movement. For translational motion these are

$$\vec{x} = \vec{x}_0 + \vec{v}t + \frac{1}{2}\vec{a}t^2, \tag{A.1}$$

43

$$\vec{v} = \vec{v}_0 + \vec{a}t, \tag{A.2}$$

where $\vec{x}$ is the WaferSat's position, $\vec{v}$ is its velocity, $\vec{a}$ is its acceleration, and t is the time step. The equations for rotational motion are similar:

$$\theta = \theta_0 + \omega t + \frac{1}{2}\alpha t^2, \tag{A.3}$$

$$\omega = \omega_0 + \alpha t, \tag{A.4}$$

where θ is the WaferSat's angular position between 0 and 2π radians, ω is its angular velocity in rad/s, and α is its angular acceleration in rad/s^2. Since this study only investigated motion in the x–y plane, there was assumed to be no rotation about the WaferSat's x– or y–axis, only about the z axis.

The next step was to determine the forces and torques applied to the WaferSat by the thrusters. As described by Newton's Third Law, the forces acting on the WaferSat by the thrusters acted in the opposite direction from where the thrusters are pointed. So the $+x$ thruster exerted a force in the $-x$ direction. The equation for the force exerted by a thruster on the WaferSat body is

$$\vec{F} = \left(\vec{F}_{\text{thrust}} \cdot \hat{r}\right)\hat{r}, \tag{A.5}$$

where $\vec{F}$ is the force exerted by the thruster, $\vec{F}_{\text{thrust}}$ is the thrust vector, and $\hat{r}$ is the unit vector pointing from the WaferSat's center of mass in the direction of the thruster. All of these vectors were in the WaferSat's body frame, in which the origin was located at the center of mass, also assumed for simplicity to be the WaferSat's geometric center. The torque exerted by a thruster is

$$\vec{T} = \vec{r} \times \vec{F}_{\text{thrust}}, \tag{A.6}$$

where $\vec{T}$ is the torque, and $\vec{r}$ is the vector from the WaferSat's center of mass to the thruster. From the forces and torques exerted by the thrusters, the translation and

rotational accelerations of the WaferSat were calculated using

$$\vec{a} = \frac{\vec{F}}{m},$$ (A.7)

$$\alpha = \frac{T}{I_z},$$ (A.8)

where m is the mass of the WaferSat and I_z is its moment of inertial about the z axis. Because the rate of fuel used in electrospray propulsion is very low, the mass of the WaferSat was assumed to be constant throughout its lifetime. The equation for the moment of inertia of a thin disk about its z axis is $I_z = \frac{1}{2}mR^2$, where R is the radius of the disk. Using Equations A.1 to A.8, the state vector of the center of mass and the rotation of the WaferSat could then be calculated. The translational and rotational accelerations due to the thrusters firing were calculated at a given point in time, then they were used to calculate the translational and rotational velocities, and finally the translational and rotational positions. The state vector was then updated and used as the initial state to propagate the motion of the WaferSat forward to the next time step.

These equations of motion were coded into MATLAB as a trajectory simulation. The initial iteration of the code only allowed for a single thruster to be fired for a chosen amount of time. The code was then expanded to allow for a sequence of firing commands. The user inputted a series of firing durations and a thruster or thrusters to be fired for each firing duration. This allowed for a more accurate simulation of the WaferSat's behavior, because it would need to fire more than one thruster during a mission. The WaferSat motion simulation code propagated the WaferSat's state through the desired firing sequence and outputted plots of the WaferSat's trajectory and state variables.

Four examples of firing sequences and the resulting trajectories are given below. In the first example, the thrusters were directed purely radially and there was no angular rotation. The WaferSat started with its center of mass at the origin of an inertial "lab" frame with $\theta = 0$, no translational or rotational velocity, and no translational or rotational acceleration. First, Thruster 1, pointed in the $+x$ direction, fired for

10 hours. Then, the WaferSat coasted with no thruster firing for 10 hours. Finally, Thruster 2, pointed in the $-y$ direction, fired for 10 hours. In all, the WaferSat moved approximately 1,000 km from its initial position. Its trajectory is shown in Figure A-7. The green dot denotes the WaferSat's starting position and the red dot denotes its final position. The blue dots indicate when a new thruster started firing. As expected, the WaferSat initially moved in the $-x$ direction. In the last 10 hours it continued to move in the $-x$ direction because of the velocity initially imparted on it by Thruster 1, but also moved in the $+y$ direction. Although this distance traveled
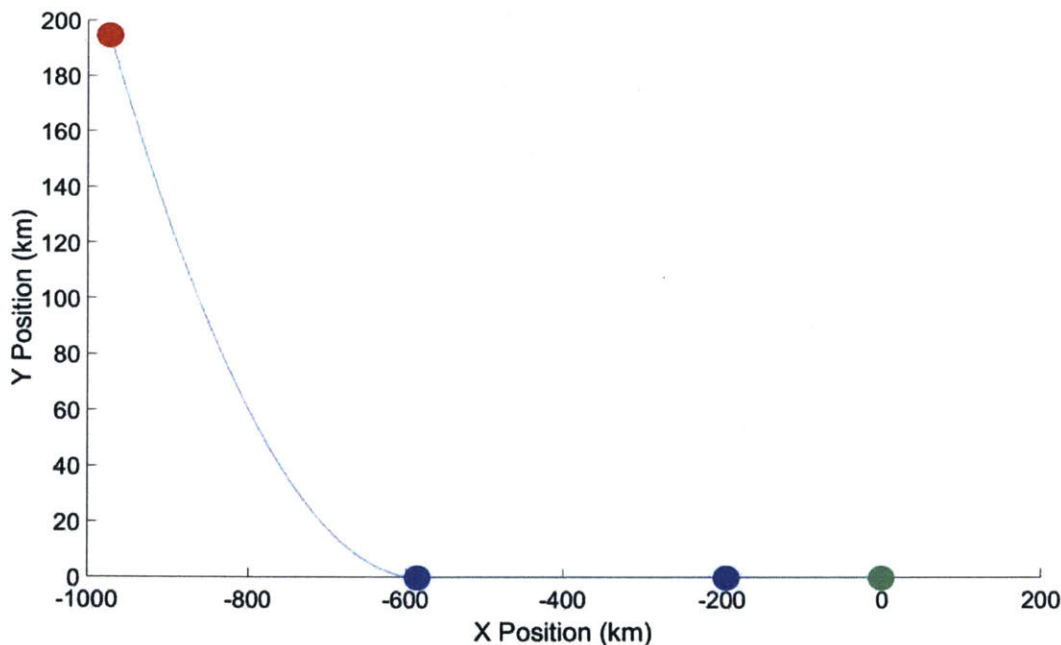

Figure A-7: WaferSat motion example 1.

by the WaferSat in this example is not much less than the semi-major axis of a LEO orbit, the assumption of a 2-D plane was still used so that this example acts as a baseline for later more complex examples.

In the second example, the WaferSat thrusters were still radially directed, but now the WaferSat had a constant angular velocity of 10^{-3} rad/s, or about 0.01 RPM. Thruster 1 initially fired for 10 hours, then Thruster 2 fired for 30 hours, and finally Thruster 3 fired for 10 hours. The WaferSat's trajectory is shown in Figure A-8. The

constant angular velocity caused the WaferSat to move in a scalloping motion, as the thruster vectors continually changed direction in the inertial frame. It also resulted in the WaferSat travelling a significantly shorter overall distance than in the previous example, despite this simulation being 20 hours longer.
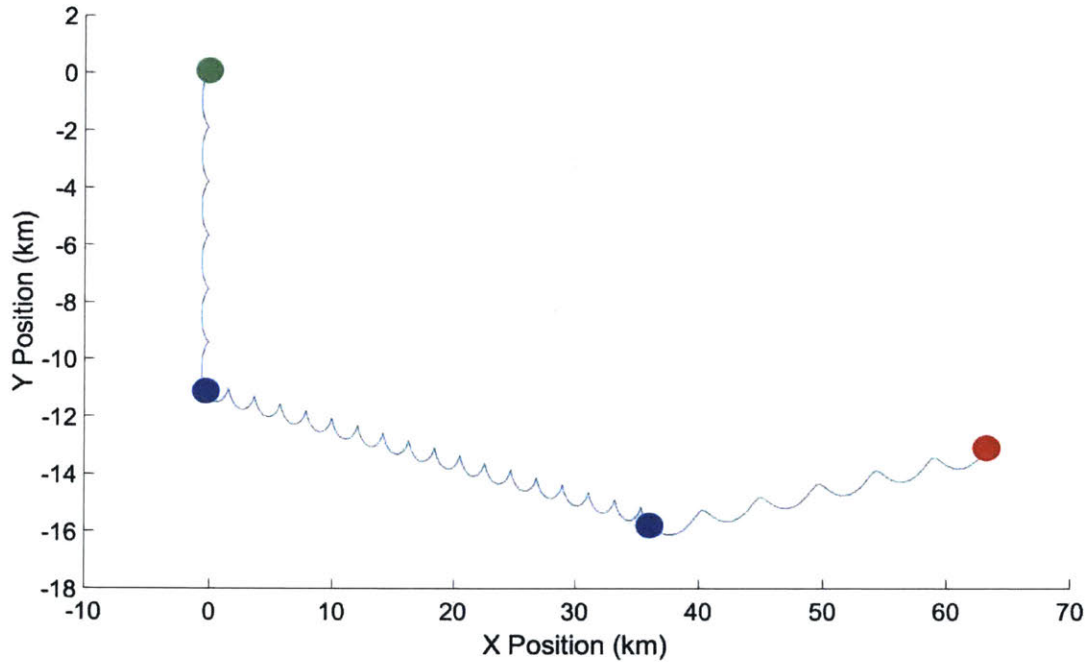

Figure A-8: WaferSat motion example 2.

In the final two simulations, the four thrusters were pointed away from the radial direction. In the third example, the WaferSat started with no angular velocity, but the thrust vectors were directed at $45°$ from the WaferSat's $x-$ and $y-$axes as shown in Figure A-9.
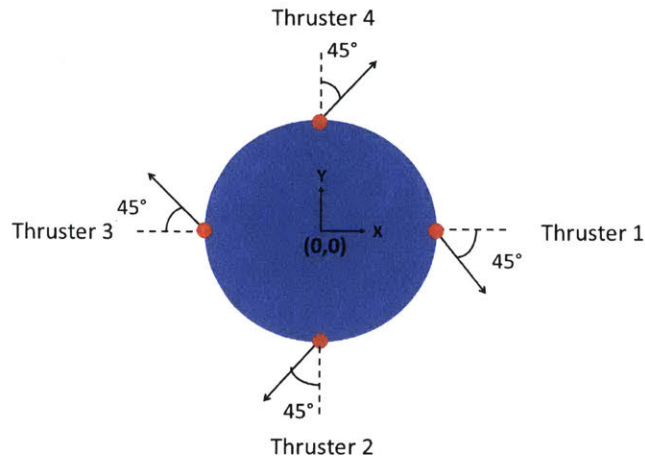
Figure A-9: WaferSat with thrust vectors directed at $45°$

The firing sequence was the same as in the first example: Thruster 1 fired for 10 hours, followed by the WaferSat coasting for 10 hours, and then finally Thruster 2 fired for 10 hours. The resulting trajectory is shown in Figure A-10. The WaferSat moved in the same general direction as in the first example, but for a drastically shorter overall distance. In this example, it moved in a diagonal line approximately 0.5 km. The scalloping motion from the previous example was not present here. Instead, the WaferSat "spun up". Initially, it moved in a wave pattern, but it quickly spin stabilized and then moved in a straight line.
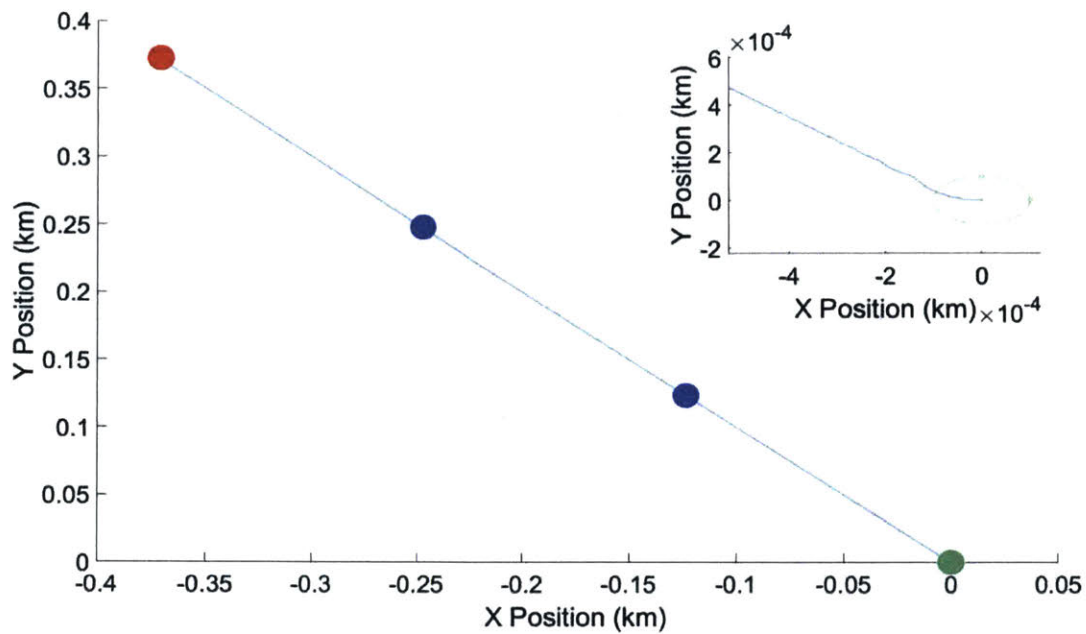
Figure A-10: WaferSat motion example 3.

The final example involved a WaferSat with tangentially directed thrusters, as shown in Figure A-11, and no initial angular velocity. This case served as a check that the simulator functioned as expected.
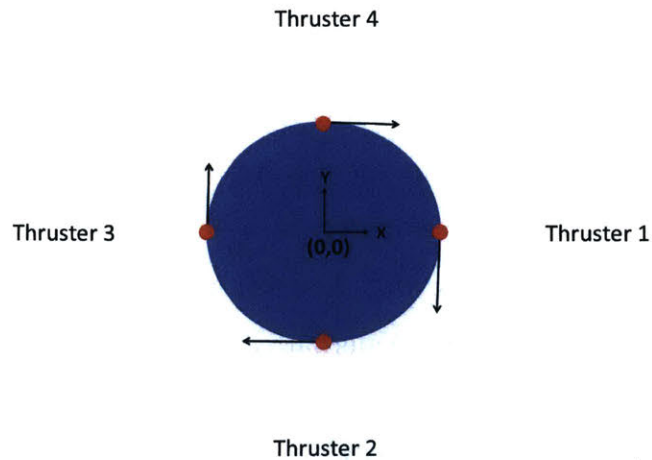

Figure A-11: WaferSat with tangentially directed thrust vectors

The firing sequence was the same as in the previous example. As expected, the

motion of the WaferSat was purely rotational, as shown in Figure A-12. This figure simply shows the outline of the WaferSat, since it only rotated about its center of mass and did not experience any translational motion.
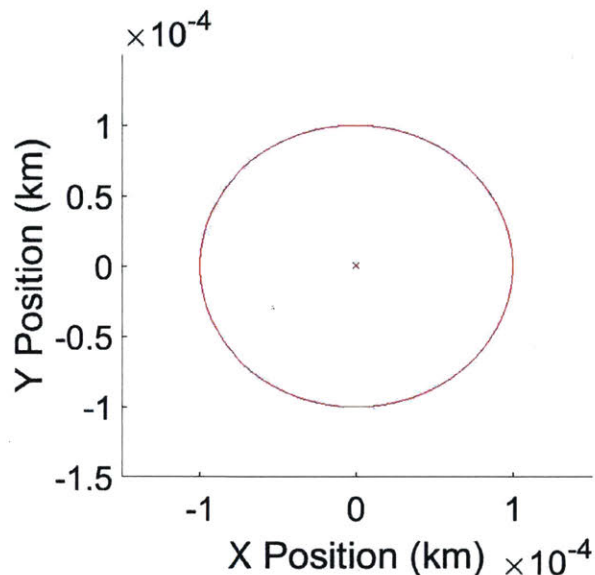

Figure A-12: WaferSat motion example 4.

The first and last examples confirmed that the state propagator correctly propagated the WaferSat's motion. However, the second and third examples revealed an important need of the WaferSat bus. In the third example, the WaferSat spun up to an angular velocity of ~300 rad/s, or about 48 revolutions per second (~2900 RPM). This is too high for the silicon wafers to withstand. Therefore, the WaferSat will need an accelerometer to monitor its angular velocity. If the angular velocity does approach its limit, another thruster would need to be fired to reduce the angular velocity. Induced angular velocity will therefore need to be taken into account in mission planning to ensure that the WaferSat can move to the desired location.

A.2.2   Sensitivity to Offset Thrust Vectors

When WaferSats are fabricated, due to the imperfections in the fabrication and assembly processes, the thrust vectors of the in-plane thrusters will be offset from the radial direction by an as-yet unkown amount. As shown in the third example in the

previous section, a large thrust vector offset has a dramatic effect on the trajectory of the WaferSat. However, offset thrust vectors due to machining imperfections are not expected to be as large 45° off radial. Instead, thrust vector offsets are expected to be a few degrees or less. Therefore, the next step in this study was to do a sensitivity analysis. Thrust vector offsets of 0.0001°, 0.001°, 0.01°, 0.1°, and 1° were run through the WaferSat motion simulation and compared to the 0° offset case, the first example in the previous section. In each case all four thrust vectors were offset by the same amount and in the same direction, as shown in Figure A-13, where θ is the degree of offset between 0° and 1°. The firing sequence for this sensitivity analysis was the same as for the first example in the previous section. First, Thruster 1 fired for ten hours, then the WaferSat coasted for ten hours, and finally Thruster 2 fired for ten hours. Results will be presented first, followed by a discussion of the patterns and observations.
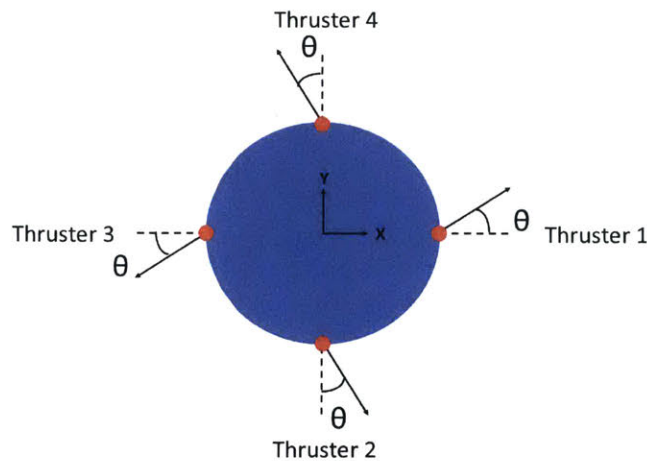

Figure A-13: Thrust vector offset.

The first test case in this sensitivity analysis was the 0.0001° thrust vector offset. The trajectory, shown in Figure A-14, was in the same general direction as in the case with no thrust vector offset. The thruster moved in the $-x$ and $+y$ directions. However, unlike in the case of purely radially directed thrust vectors, the WaferSat

in this case moved diagonally for the entire simulation. This change in trajectory shape was due to the torque from the offset thrust vectors. The torque induced an angular rotation of the WaferSat about its center of mass, and as the WaferSat rotated, the positions of the thrust vectors in the inertial frame constantly changed. Because the thrust vectors were very slightly offset from radial, the WaferSat only experienced a small torque and rotated slowly. The WaferSat moved 350 km from its initial position, which is approximately 36% of its displacement in the case of 0° offset. It moved 20 km less in the y direction, but 700 km less in the x direction. Noticeably, the WaferSat in this case moved in a wave-like motion, caused by its slow rotation. This wave motion was not present during the ten hours of coasting, and decreased in the last ten hours as Thruster 2 fired, and the rotation rate increased.
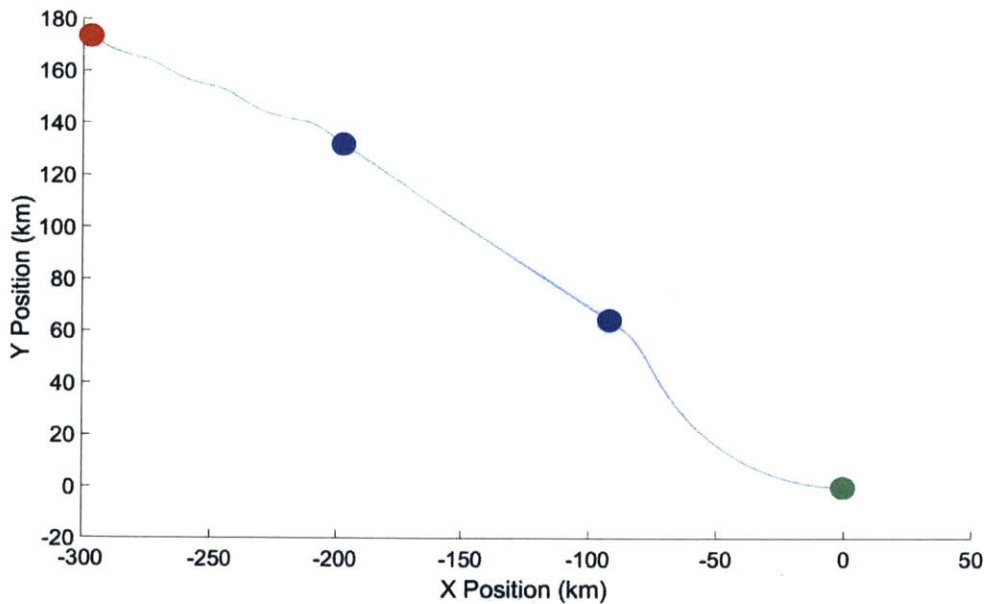
Figure A-14: Trajectory of WaferSat with 0.0001° thrust vector offset.

The next test case was a 0.001° offset in thrust vectors. As shown in Figure A-15, this trajectory moved in the same diagonal direction as in the previous test case. However, because the thruster offset was greater and the resulting torque was larger, the wave motion was much smaller and almost disappeared in the final ten hours. In

this case, the WaferSat was displaced 120 km, which was approximately 12% of its displacement in the 0° offset case.
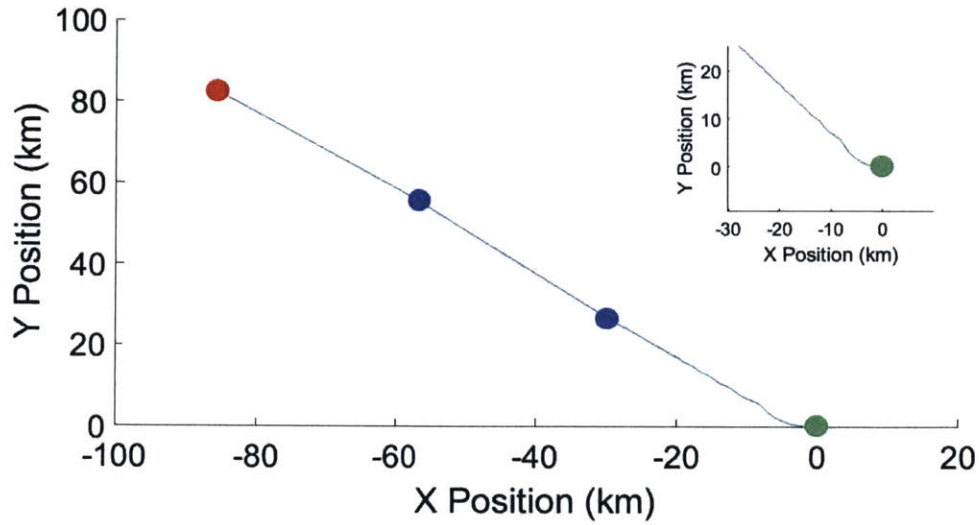
Figure A-15: Trajectory of WaferSat with 0.001° thrust vector offset.

The third test case was a 0.01° thrust vector offset. The wave like motion seen in the previous cases was barely present in this case, even during the WaferSat's initial movement. The WaferSat's trajectory in this case is shown in Figure A-16. Once again, it moved in a diagonal trajectory, but in this case it was only displaced 40 km, 4% of the displacement in the 0° offset case.

Figure A-16: Trajectory of WaferSat with 0.01° thrust vector offset

The fourth test case in this sensitivity analysis was a 0.1° offset. In this case, the wave motion was virtually unobservable, except in the initial movement of the WaferSat. A plot of the WaferSat's trajectory in this case is shown in Figure A-17. Again, the WaferSat moved in a diagonal line. However, in this case, it was displaced only 12 km, approximately 1% of the displacement in the 0° offset case.

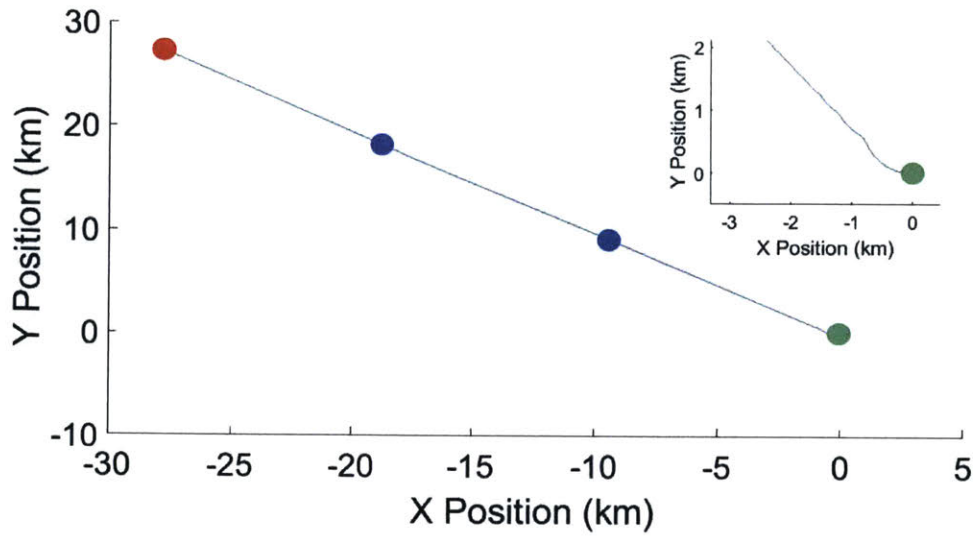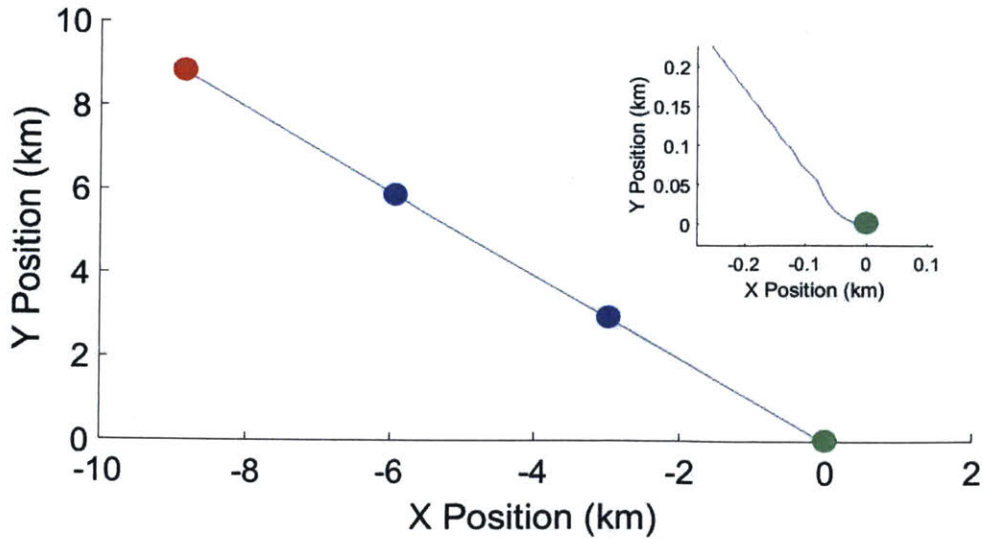Figure A-17: Trajectory of WaferSat with 0.1° thrust vector offset.

The final test case in the sensitivity analysis was a 1° offset. In this final test case there was virtually no discernable wave motion, as shown in the trajectory in Figure A-18. As in the previous test cases, the WaferSat moved in a diagonal direction. In this case it was displaced only 4 km, 0.4% of the displacement in the 0° offset case.
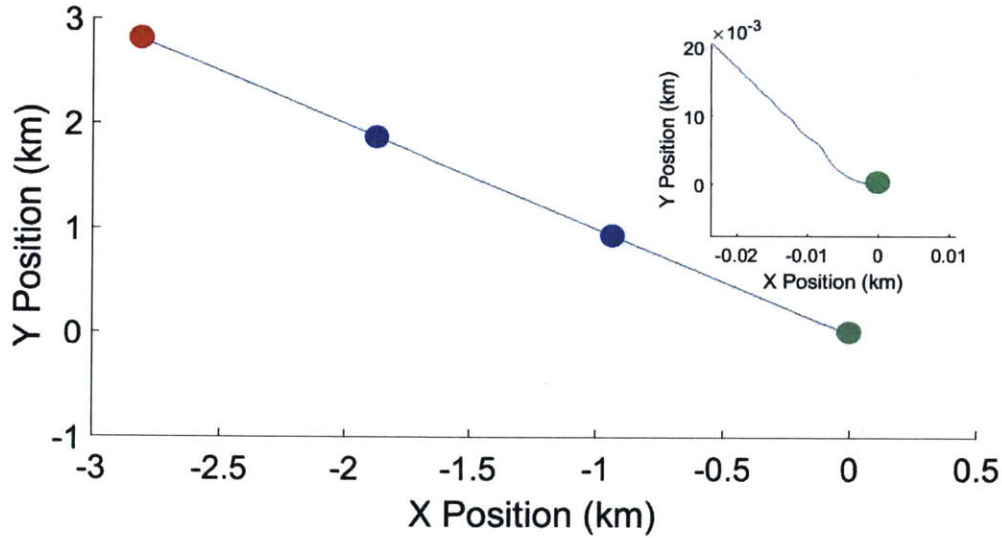
Figure A-18: Trajectory of WaferSat with 1° thrust vector offset.

The results of the sensitivity analysis are summarized in Table A.1.

Table A.1: Thrust Vector Offset Summary

θ Offset	X Displacement (km)	Y Displacement (km)	Fraction of Baseline Displacement (%)	Observations
0°	-950	190	100%	baseline
0.0001°	-290	170	36%	large waves
0.001°	-85	82	12%	smaller waves
0.01°	-27	27	4%	very small waves
0.1°	-8.7	8.7	1%	waves not noticeable
1°	-2.7	2.7	0.4%	waves not noticeable

From these five test cases, it was apparent that even a small misalignment in thruster placement had a drastic effect on both the displacement of the WaferSat and

the motion of its trajectory. In fabrication, it will be important to keep the thrust vectors as close to radially directed as possible. Additionally, the thrust vector offset for each thruster will need to be calibrated, so that the effect of the offsets on the WaferSat's motion can be predicted. In all five test cases, the WaferSat spun up, similarly to its behavior in the third test case in the previous section. Greater thrust vector offsets created more torque on the WaferSat, which in turn led to a higher rotational acceleration α. This caused the WaferSat to spin up faster and move in less of a wave motion as the offset increased. Another important discovery from this sensitivity analysis is that even for thrust vector offsets of less than $1°$, the torque can quickly result in high ω. However, if a WaferSat spins too quickly, parts of the satellite will fly off the silicon wafer body and the satellite will break apart. Since α is dependent on I_z, which is in turn dependent on the mass of the WaferSat, increasing the mass of the WaferSat should decrease its sensitivity to offset thrust vectors.

A.2.3 Thruster Control Optimization Using a Genetic Algorithm

Mission planning requires determining a thruster firing sequence to take the satellite from a known location to a different, desired location. Therefore, the focus of this study shifted from observing the results of a firing sequence to finding the "best" firing sequence to move the WaferSat between two points. Seen as an optimization problem, determining the optimal firing sequence has both integer constraints (which thrusters to fire) and continuous constraints (how long to fire them). The genetic algorithm (GA) is an optimization method that handles both integer and continuous constraints. For this study, the GA routine provided by the MATLAB Global Optimization Toolbox was used with its default parameters. This section describes a study of the use of the GA to automatically determine the optimal firing sequence to achieve a certain motion of the WaferSat. While it used a simple model without gravity or drag and only simple motion, I believe the lessons learned, which are presented below, will make the GA useful for determining control sequences under realistic orbital conditions.

The GA optimization process consisted of a series of steps. First, the desired

number of "firing commands" was set. A firing command was a choice of zero, one, or multiple thrusters to fire simultaneously and a duration to fire (or not fire) for. Originally this was set to a sequence of four commands, but was later expanded to seven to give the GA more options. Next, an upper bound was set on the duration of a single firing command. A cost function was written to dictate what constituted the "best" firing sequence. Three factors were included in the cost function: the accuracy of the trajectory (the difference between the WaferSat's simulated final state vector and the desired final state vector), the amount of fuel used, and the time the WaferSat took to arrive at its final location. The cost function for the optimization was a combination of individual cost functions for each of these three factors. The cost function for the state was the Euclidean distance between the actual final state vector and the desired final state vector,

$$C_{state} = \left((\vec{x}_{\text{desired}} - \vec{x}_{\text{actual}})^2 + \left(\dot{\vec{x}}_{\text{desired}} - \dot{\vec{x}}_{\text{actual}} \right)^2 + \left(\ddot{\vec{x}}_{\text{desired}} - \ddot{\vec{x}}_{\text{actual}} \right)^2 + \\ (\theta_{\text{desired}} - \theta_{\text{actual}})^2 + (\omega_{\text{desired}} - \omega_{\text{actual}})^2 + (\alpha_{\text{desired}} - \alpha_{\text{actual}})^2 \right)^{\frac{1}{2}}. \tag{A.9}$$

The cost function for time was simply the total time the WaferSat took to move to its final location,

$$C_{time} = \frac{\text{time}_{\text{sim}}}{\text{tol}}. \tag{A.10}$$

The cost function for fuel used was the total amount of time thrusters were firing multiplied by an estimated rate of fuel usage,

$$C_{fuel} = \frac{\sum \dot{m}t}{\text{tol}}. \tag{A.11}$$

The three cost functions were then combined into a single overall cost function as

$$C = \sqrt{(XC_{\text{state}})^2 + (YC_{\text{time}})^2 + (ZC_{\text{fuel}})^2}. \tag{A.12}$$

Each individual cost function was assigned a coefficient, X, Y, or Z. These coefficients ensured that the individual cost functions were not just the same order of magnitude,

but that they were also approximately equally weighted. In further experiments, these coefficients were varied by two or more orders of magnitude to determine their relative impact on the results of the optimization.

The optimization procedure consisted of letting the GA choose firing command sequences and run the simulation to determine how well the firing command sequence produced the desired motion. The GA was run first with a coarse simulation time step, then the results were fed into another GA run with a medium simulation time step, then again with a fine time step. This was found to improve the speed of the optimization process and the quality of the results. Typical coarse, medium, and fine time steps were 30 s, 10 s, and 1 s, respectively. Because the GA is a randomized algorithm, the results of multiple GA runs were compared against each other.

The test case used in this study was to have the WaferSat start from a stationary position and move 1 km in the $+y$ direction, with zero final velocity, acceleration, and rotation. The WaferSat mass was 50 g and it had four equally spaced radially directed thrusters as previously described, with no angular offsets. A naïve first guess solution was to have Thruster 2 fire to move the WaferSat in the $+y$ direction and then to fire Thruster 4 to slow down the WaferSat so that it arrived at the end point with zero velocity. While the GA did give many solutions that followed this pattern, it also occasionally, randomly gave firing sequences that included nonsensical firing commands such as firing all four thrusters at once or firing two opposing thrusters at once. These nonsensical commands were removed from the selection of available firing command options for the purpose of this test case. However, in future work involving non-radially directed or misaligned thrusters, some of these firing commands may need to be added back in.

Table A.2 shows initial example results of the firing sequences from the GA when only the coarse time step of 30 s was used. In this and future tables, the final rotational parameters are omitted, because they were always identically zero. These initial results were obtained with the coarse time step only; later experiments used finer time steps for greater fidelity. The middle column shows the final state vector when all three factors — state, time, and fuel — were equally weighted in the GA's

cost function. The right column shows the results when time was weighted higher than the other factors in the cost function. In both cases, the final position of the WaferSat was the same. However, when time was emphasized, the residual final velocity of the WaferSat was higher, and the resulting firing command sequence used an order of magnitude more fuel. The firing command sequences found by the GA were similar to the naïve solution, following the pattern of either "gas then brake" or "gas, coast, then brake". In the case when time was emphasized, the WaferSat coasted for a shorter time, allowing it to reach its final destination faster, but at the cost of using more fuel.

Table A.2: Example GA Outputs

	Equal Weights	Time Emphasized
Final x (m)	0	0
Final y (m)	1000.08	1000.08
Final $\dot{x}$ (m/s)	0	0
Final $\dot{y}$ (m/s)	0.09	0.252
Final $\ddot{x}$ (m/s^2)	0	0
Final $\ddot{y}$ (m/s^2)	0	0
Time	11400 s (3.2 hours)	3000 s (0.8 hours)
Fuel Used (mg)	2.584	27.273

For WaferSat missions, final position and velocity will be especially important. Each WaferSat will need to be in a specific location within a swarm or constellation, and a low relative velocity will help keep the WaferSat from drifting from its location. Because the GA is randomized, it sometimes produces suboptimal results. So the optimization procedure was run repeatedly until the final state was within 10 m of the desired final position and the final velocity was less than 1 mm/s. I was unable to force the GA to produce results consistently within these bounds by modifying the form or weights of the cost function, hence the need to run the optimizer repeatedly until an acceptable result was obtained.

Initially, the GA used only a 30 s time step. However, re-running the final firing solution through the femtosatellite motion simulation outside of the loop with a time step of 0.01 s showed that the "acceptable" solutions could actually be up to 100 m off from the desired location. Table A.3 below shows one such example, with the final state as predicted by a 30 s time step vs. the final state as calculated by a 0.01 s time step for the same firing sequence.

Table A.3: Error Due to Simulation Time Step

	30 s Time Step	0.01 s Time Step
Final x (m)	0	0
Final y (m)	994.68	909.68
Final $\dot{x}$ (m/s)	0	0
Final $\dot{y}$ (m/s)	0.09	-0.0069
Final $\ddot{x}$ (m/s^2)	0	0
Final $\ddot{y}$ (m/s^2)	0	0

To resolve this discrepancy, the coarse time step was decreased to 10 s, and the additional GA runs with medium and fine time steps of 1 s and 0.01 s, respectively, were added to the procedure as described above. These additions consistently gave firing sequences that resulted in acceptable final states within the boundaries imposed on position and velocity. An example is shown below in Table A.4.

Table A.4: Simulation Results With Additional GA Runs

	30 s Time Step Only	With 1 s Time Step	With 0.01 s Time Step
Final x (m)	0	0	0
Final y (m)	999.75	1000.02	997.80
Final $\dot{x}$ (m/s)	0	0	0
Final $\dot{y}$ (m/s)	0	0	-0.00018
Final $\ddot{x}$ (m/s^2)	0	0	0
Final $\ddot{y}$ (m/s^2)	0	0	0

Although these time steps produced good results for the case of translational motion and no angular velocity, the optimization process took a long time to run. Future

cases with offset thrusters, angular velocity, or a combination of the two will require smaller time steps. One possible improvement is to rewrite the femtosatellite motion simulation code to use an ordinary differential equation solver such as MATLAB's ode45 which uses a variable time step.

A.3   Conclusion

This study was useful for developing thruster firing commands to give to a WaferSat to move it a short distance in a 2-D plane. Commands to change the WaferSat's orbital elements, specifically the semi-major axis and orbital inclination, were not studied. This study gave useful insights into WaferSat motion that inform control system design and mission planning for satellites of this general shape. WaferSats will need onboard accelerometers to monitor angular velocities, carefully calibrated thrust vectors, and control systems to compensate for rotation. From the sensitivity analysis in Section A.2.2, it became apparent that a 50 g WaferSat is particularly sensitive to thruster angular offsets. Care should be taken to ensure that thrusters would be as close to radially directed as possible. The final iteration of the GA code used in this study required parallel computing and required a significant amount of time to output an acceptable solution. It would probably be prohibitive to have each WaferSat run a program similar to the GA code described in Section A.2.3 every time it needs to move. Instead the individual WaferSats could hold in their memory a pre-calculated set of commands for their most common simple movements, and a mothership or ground station could determine the firing sequence for rarer or more complex movements.

Future work on this project could include rewriting the WaferSat motion simulation to use a variable time step, moving to a 3-D simulation of the WaferSat bus, and expanding the motion simulation from a plane to a more realistic orbital force model. The variable time step can be added into the WaferSat motion simulation by using a more advanced ordinary differential equation solver. A 3-D model of a WaferSat will most likely involve a change in coordinate system from a Cartesian body frame

to one such as Euler angles. This would also necessitate additional calculations to move between Euler angles in the WaferSat body frame and a different coordinate system in the inertial frame. A more realistic simulation will include at least a simple orbital motion model with no perturbations. Later versions of the simulation should be expanded to include perturbations due to atmospheric drag, solar radiation pressure, and other effects. These areas of future work will bring greater fidelity to the WaferSat motion model and better inform the design of the WaferSat propulsion and control systems.

Bibliography

[1] P. C. Lozano. Fluoro-hydrogenated ionic liquids (FHIL) for high-performance electrospray propulsion. AFOSR Funding Proposal.

[2] C. Coffman, M. Martínez-Sánchez, F. J. Higuera, and P. C. Lozano. Structure of the menisci of leaky dielectric liquids during electrically-assisted evaporation of ions. *Applied Physics Letters*, 109(23), December 2016.

[3] R. Hagiwara, K. Matsumoto, Y. Nakamor, T.Tsunda, Y. Ito, H. Matsumoto, and K. Momota. Physicochemical properties of 1,3-dialkylimidazolium fluorohydrogenate room-temperature molten salts. *Journal of The Electrochemical Society*, 150(12):D195–D199, 2003.

[4] R. Taniki, K. Matsumoto, and R. Haiwara. Trialkylsulfonium fluorohydrogenate giving the highest conductivity in room-temperature ionic liquids. *Electrochemical and Solid-State Letters*, 15(4):F13–F15, 2012.

[5] P. C. Lozano. iEPS thrust density plot. MIT SPL memo to AFOSR.

[6] P. C. Lozano. Fluoro-hydrogenated ionic liquids (FHIL) for high-performance electrospray propulsion. Extended Abstract, 2017 AFOSR Space Propulsion Program Review.

[7] P. C. Lozano. 16.522 lecture 20: Electrospray propulsion. $https : //ocw.mit.edu/courses/aeronautics-and-astronautics/16-522-space-propulsion-spring-2015/lecture-notes/MIT16\_522S15\_Lecture20.pdf$, 2015.

[8] P. C. Lozano. 16.522 lecture 24: Ion emission and the pure ionic regime. $https : //ocw.mit.edu/courses/aeronautics-and-astronautics/16-522-space-propulsion-spring-2015/lecture-notes/MIT16\_522S15\_Lecture24.pdf$, 2015.

[9] G. Taylor. Disintegration of water drops in an electric field. *Proceedings of the Royal Society of London. Series A, Mathematical and Physical Sciences*, 280(1382):383–397, July 1964.

[10] C. S. Perez-Martinez. *Engineering Ionic Liquid Ion Sources for Ion Beam Applications.* PhD dissertation, Massachusetts Institute of Technology, Department of Aeronautics and Astronautics, June 2016.

[11] I. Romero-Sanz, R. Bocanegra, J. Fernandez de la Mora, and M. Gamero-Castaño. Source of heavy molecular ions based on Taylor cones of ionic liquids operating in the pure ion evaporation regime. *Journal of Applied Physics*, 94(5):3599–3605, September 2003.

[12] T. M. Coles and P. C. Lozano. Investigating efficiency losses rom solvated ion fragmentation in electrospray thruster beams. 49th Annual AIAA/ASME/SAE/ASEE Joint Propulsion Conference, San Jose, CA, July 2013.

[13] P. C. Lozano. 16.522 lectures 22-23: Colloid thrusters. $https : //ocw.mit.edu/courses/aeronautics - and - astronautics/16 - 522 - space - propulsion - spring - 2015/lecture - notes/MIT16\_522S15\_Lecture22 - 23.pdf$, 2015.

[14] Z. Zhou, H. Matsumoto, and K. Tatsumi. Low-viscous, low-melting, hydrophobic ionic liquids: 1-alkyl-3methylimidazolium trifluoromethyltrifluoroborate. *Chemistry Letters*, 33(6):680–681, May 2004.

[15] C. E. Miller. On the stability of complex ions in ionic liquid ion sources. Master's thesis, Massachusetts Institiute of Technology, Department of Aeronautics and Astronautics, June 2013.

[16] D. J. Barnhart, T. Vladimirova, and M. N. Sweeting. System-on-a-chip design of self-powered wireless sensor nodes for hostile environments. 2007 IEEE Aerospace Conference, Big Sky, MT, March 2007.

[17] J. Keller interview with A. Joshi. Startup to develop satellite-on-a-chip, February 1994.

[18] S. W. Janson. Mass-producible silicon spacecraft for 21st century missions. AIAA Space Technology Conference and Exposition, Albuquerque, NM, September 1999.

[19] D. J. Barnhart. *Very Small Satellite Design for Space Sensor Networks*. PhD dissertation, University of Surrey, Faculty of Engineering and Physical Sciences, Surrey Space Centre, June 2008.

[20] S. Chung and F. Y. Hadaegh. Swarms of femtosats for synthetic aperture applications. 4th International Conference on Spacecraft Formation Flying Missions and Technologies, St. Hubert, Quebec, May 2011.

[21] F. Y. Hadaegh, S. Chung, and H. M. Manohara. On development of 100-gram-class spacecraft for swarm applications. *IEEE Systems Journal*, 10(2):673–684, August 2016.

[22] Z. Manchester, M. Peck, and A. Filo. Kicksat: A crowd-funded mission to demonstrate the world's smallest spacecraft. 27th Annual AIAA/USU Conference on Small Satellites, Logan, UT, August 2013.

[23] J. A. Atchison and M. A. Peck. A passive, sun-pointing, milimeter-scale solar sail. *Acta Astronautica*, 67(1-2):108–121, 2010.

[24] Z. Manchester. Kicksat – your personal spacecraft in space! Blog. $https://www.kickstarter.com/projects/251588730/kicksat-your-personal-spacecraft-in-space/posts$.

[25] M. Smith. MIT Lincoln Laboratory internal proposal, 2017.